Top of the Atmosphere Reflected Shortwave Radiative Fluxes from GOES-R

Rachel T. Pinker[1], Yingtao Ma[1], Wen. Chen[1], Istvan Laszlo[2], Hongqing Liu[3], Hye-Yun Kim[3] and Jamie Daniels[2]

[1] Department of Atmospheric and Oceanic Science, University of Maryland, College Park, MD

[2] NOAA NESDIS Center for Satellite Applications and Research, College Park, MD

[3] I.M. Systems Group, Inc., Rockville, MD

Correspondence to: Rachel T. Pinker (pinker@atmos.umd.edu)

Abstract. Under the GOES-R activity, new algorithms are being developed at the National Oceanic and Atmospheric Administration (NOAA)/Center for Satellite Applications and Research (STAR) to derive surface and Top of the Atmosphere (TOA) shortwave (SW) radiative fluxes from the Advanced Baseline Imager (ABI), the primary instrument on GOES-R. This paper describes a support effort in the development and evaluation of the ABI instrument capabilities to derive such fluxes. Specifically, scene dependent narrow-to-broadband (NTB) transformations are developed to facilitate the use of observations from ABI at the TOA. Simulations of NTB transformations have been performed with MODTRAN4.3 using an updated selection of atmospheric profiles and implemented with the final ABI specifications. These are combined with Angular Distribution Models (ADMs), which are a synergy of ADMs from the Clouds and the Earth's Radiant Energy System (CERES) and from simulations. Surface condition at the scale of the ABI products as needed to compute the TOA radiative fluxes come from the International Geosphere-Biosphere Programme (IGBP). Land classification at 1/6° resolution for 18 surface types are converted to the ABI 2-km grid over the (CONtiguous States of the United States) (CONUS) and subsequently re-grouped to 12 IGBP types to match the classification of the CERES ADMs. In the simulations, default information on aerosols and clouds is based on the ones used in MODTRAN.

Comparison of derived fluxes at the TOA is made with those from the CERES~~ and/or the Fast Longwave and Shortwave Radiative Flux (FLASHFlux) data~~. A~~n~~ satisfactory agreement between the fluxes was observed and possible reasons for differences have been identified**;** the agreement of the fluxes at the TOA for predominantly clear sky conditions was found to be better than for cloudy sky due to possible time shift in observation times between the two observing systems that might have affected the position of the clouds during such periods. Differences in assumed cloud properties can also lead to differences in the fluxes derived from the two instruments.

1 ~~1~~ Introduction

~~When a new satellite is contemplated, the exact characteristics of the newly selected sensors are not fully known; simulations of proposed sensors are also not readily available. Yet, there is a need to obtain a priori information on the expected performance of the new instruments. This is usually accomplished by using characteristics of instruments in closest resemblance to the proposed ones and performing simulations that can provide insight on the expected performance of the new instrument. As such, an evolutionary process can be expected~~~~precedes the final stage that is reported in this paper.~~ ~~and it did precede activities reported in this manuscript.~~ One of the objectives at ~~The ultimate objective at~~ NOAA/STAR in respect to the utilization of observations from ~~is to be able to derive shortwave (SW) radiative fluxes from~~ the Advanced Baseline Imager (ABI) is to be able to derive shortwave (SW) radiative fluxes from.~~,~~ To get to the surface SW from TOA satellite observations, there are two generic approaches: 1) the direct approach and 2) the indirect approach. In the direct approach one uses all the necessary information needed for deriving the surface fluxes (some of which can be derived from satellites). Implementation of s~~S~~uch an approach is feasible, for instance, with observations from MODIS ~~where there is~~which has a long history of product availability and evaluation. Examples ~~of such an approach using MODIS observation~~ are illustrated in Wang and Pinker (2009), Ma et al. (2016), Pinker et al. (2018), Pinker et al., (2017a), Pinker et al. (2017b), Niu and Pinker, (2015). GOES-R is a new instrument and as yet, similar information to the one available from

Formatted: Font: Bold, Complex Script Font: Bold

Formatted: List Paragraph, Numbered + Level: 1 + Numbering Style: 1, 2, 3, … + Start at: 1 + Alignment: Left + Aligned at: 0.25" + Indent at: 0.5"

MODIS is not yet available. Therefore, the indirect approach is used where one starts from satellite information at the TOA and models the atmosphere and surface with best available inputs (which do not have to be based on ABI). Examples of such an approach are discussed in Pinker, Zhang and Dutton (2005), Ma and Pinker (2012) and Zhang et al. (2019). The “indirect path method” is used at the Center for Satellite Applications and Research (STAR) (Laszlo et al., 2020) for deriving SW radiative fluxes from satellite observations; it requires knowledge of the SW broadband (0.2 – 4.0 µm) top of the atmosphere (TOA) albedo. The Advanced Baseline Imager (ABI) observations onboard of the NOAA GOES-R series of satellites provide ~~reflectances~~reflectance in six narrow bands in the shortwave spectrum (**Table 1**); these must be first transformed into broadband reflectance (the narrow-to-broadband, NTB, conversion process), and then the broadband reflectance must be transformed into a broadband albedo (the ADM conversion process).

During the pre-launch activity NTB transformations were developed based on theoretical radiative transfer simulations with MODTRAN-3.7 and 14 land use classifications from the International Geosphere-Biosphere Programme (*IGBP) (*Hansen et al., 2010*)*. They were augmented with ADMs from (CERES) observed ADMs (Loeb et al., 2003) and theoretical simulations (Niu and Pinker, 2011) to compute TOA fluxes. The resulting NTB transformations and ADMs have been tested using proxy data and simulated ABI data. The proxy instruments used in the simulations include the GOES-8 satellite, the Advanced Very-High Resolution Radiometer (AVHRR) sensor on the Polar Orbiting satellites, the Spinning Enhanced Visible Infra-Red Imager **(**SEVIRI) sensor on the European METEOSAT Second Generation (MSG) satellites, and the Moderate Resolution Imaging Spectroradiometer (MODIS) instrument on the NASA Terra and Aqua Polar Orbiting satellites (Pinker et al., 2021, unpublished). For each of these satellites, the evaluation of the methodologies was done differently; some results were evaluated against ground observations while others, against TOA information from CERES as well as from the (ESA) Geostationary Earth Radiation Budget (GERB) satellite (Harries et al., 2005). The results obtained provided an insight on the expected performance of the new ABI sensor. Those procedures have

Formatted: Font: 12 pt, Complex Script Font: 12 pt

Formatted: Font: 12 pt, Complex Script Font: 12 pt

Formatted: Font: 12 pt, Complex Script Font: 12 pt

Formatted: Font: 12 pt, Complex Script Font: 12 pt

Formatted: Font: 12 pt, Complex Script Font: 12 pt

Formatted: Comment Text, Indent: First line: 0", Tab stops: Not at 0.69" been subsequently updated and applied to the new ABI instrument once it was built and fully characterized.

In this paper we describe activity in support of methodologies to derive surface shortwave (SW) radiative fluxes from the operational Advanced Baseline Imager (ABI) instrument on the GOES-R series of the NOAA geostationary meteorological satellites. We describe the physical basis and the development of the (NTB) transformations of satellite observed radiances and the bi-directional corrections to be applied to the broadband reflectance to obtain broadband TOA albedo. The methodology will be presented in section 2, data used are described in section 3, results in section ~~3~~ 4 and a summary and discussion in section 5.

Formatted: Line spacing: 1.5 lines

2. Methodology

The following two flowcharts (**Figs. 1 and 2**) describe the necessary steps to derive the NTB transformations and the ADMs. Details of these two steps will follow.

The TOA narrowband and broadband reflectances can be calculated from the spectral radiances simulated from MODTRAN 4.3 and the response functions of the satellite sensor as shown in equations (1) and (2):

$$\rho_{nb}(\theta_0,\theta,\phi) = \frac{\pi \int_{\lambda 1}^{\lambda 2} I(\lambda,\theta_0,\theta,\phi) G(\lambda) d\lambda}{\int_{\lambda 1}^{\lambda 2} \cos(\theta_0) S_0(\lambda) G(\lambda) d\lambda} \quad (1)$$

$$\rho_{bb}(\theta_0,\theta,\phi) = \frac{\pi \int_{0.2\mu m}^{4\mu m} I(\lambda,\theta_0,\theta,\phi) d\lambda}{\int_{0.2\mu m}^{4\mu m} \cos(\theta_0) S_0(\lambda) d\lambda} \quad (2)$$

where ρ_{nb} is narrowband reflectance; ρ_{bb} is broadband reflectance; θ_0: solar zenith angle; θ: view (satellite) zenith angle; ϕ: relative azimuth angle;

I_λ: reflected spectral radiance; $S_0(\lambda)$: solar spectral irradiance;

G_λ: spectral response functions of satellite sensors; λ_1 and λ_2 are the spectral limits of the sensor spectral band. This approach is widely used in the scientific community as also implemented in the work of Loeb et al (2005), Wielicki et al. (2008), Su et al. (2015) and Akkermans et al. (2020).

As stated previously, the ADMs from CERES-based observations (Loeb et al., ~~2003~~2005; Kato et al. 2015) were augmented with theoretical simulations (Niu and Pinker, 2011) to compute TOA fluxes. This was done since ~~due to the fact that~~ CERES observations at that time ~~higher latitudes are~~ were under-sampled. ~~or not existent.~~ at higher latitudes.

The combined ADMs are developed for each angular bin by weighting the modeled and CERES ADMs based on the number of samples used to derive the ADMs of each type (Niu et al., 2011). Specifically:

$$\overline{R}(\theta_0,\theta,\phi) = \frac{1}{m+n}\left(m \times R_{CERES}(\theta_0,\theta,\phi) + n \times R_S(\theta_0,\theta,\phi)\right) \qquad (3)$$

$\overline{R}(\theta_0,\theta,\phi)$: averaged ADMs at each angular bin;

R_{CERES}: anisotropic factor from CERES ADMs;

R_S: anisotropic factor from simulated ADMs;

m and n: observation numbers at angular bins for CERES and simulated ADMs.

2.1 Selection of Atmospheric profiles for simulations

We have selected 100 atmospheric profiles covering the globe and the seasons, to use as input for simulations with MODTRAN4.3. A tool was developed to select profiles from a Training Data set known as SeeBor Version 5.0 (https://cimss.ssec.wisc.edu/training_data/) (Borbas et.al. 2005). Originally it consisted of 15704 global profiles of temperature, moisture, and ozone at 101 pressure levels for clear sky conditions. The profiles are taken from NOAA-88, and the European Centre for Medium-Range Weather Forecasts (ECMWF) 60L training set, TIGR-3, ozone-sondes from 8 NOAA Climate Monitoring and Diagnostics Laboratory (CMDL) sites, and radiosondes from the Sahara Desert during 2004. A technique to extend the temperature, moisture, and ozone profiles above the level of existing data was also implemented by the providers (University of Wisconsin-Madison, Space Science and Engineering Center, Cooperative Institute for Meteorological Satellite Studies (CIMSS). **Fig. 3** shows the selected profile locations; each season includes 25 profiles.

The SeeBor profiles are clear sky profiles. The top of the profiles is at 0.005 mb which is about 82.6 km. We did an experiment to check the impact of reducing the number of levels for a profile (initially, we have used only 40 levels). In the experiment computed were radiances from profiles with 50 levels as well as radiances from profiles with 98 Levels. The difference between the two radiances (50 lev-98 lev) were below 5 % reaching 15 % around 2.5 μm. In the experiment we used the odd number levels starting from surface (plus the highest level) to reduce the number of profile levels. Based on these experiments we have opted to keep all 98 profile levels.

The atmospheric profiles at each pressure level include temperature, water vapor and ozone. The surface variables include surface skin temperature, 2 m temperature, land/sea mask, and albedo. We have conducted a thorough investigation how the selected profiles represent the entire sample of 15704 profiles. An example showing the comparison of temperature, humidity and ozone profiles is shown in **Fig. 4.** As seen, there is a positive bias in the selected profile of temperature due to their higher concentration at the lower latitudes. A positive bias can be found at the lower levels while a negative bias is seen above 1 mb. Since our domain of study is in such latitudes this selection should not have adverse effects on the simulations.

2.2 Surface conditions

Surface condition is one of the primary inputs into the MODTRAN simulations. The International Geosphere-Biosphere Programme (IGBP) land classification is used as data source (Hansen et al., 2010; Loveland et al., 2010). The dataset is at 1/6-degree resolution and includes 18 surface types. We have converted the $1/6^{o}$ (~18.5 km) resolution to the ABI 2-km grid using the nearest grid method **(Fig. 5)**. The surface type is fixed in time. The method for cloudy sky uses 4 surface types; these are also derived from 12 IGBP types (**Table 2**).

2.3 Clear and cloudy sky simulations

Under clear sky, ~~multiple~~ scattering from aerosols is important. We have included 6 aerosol types (**Table 3**) to cover a range of possible conditions under clear sky. Aerosol models are selected based on the type of extinction and a default meteorological range for the boundary-layer aerosol models as listed below:

Aerosol Type 1: Rural extinction, visibility = 23 km

Aerosol Type 4: Maritime extinction, visibility = 23 km

Aerosol Type 5: Urban extinction, visibility = 5 km

Aerosol Type 6: Tropospheric extinction, visibility = 50 km

Aerosol Type 8: Advective Fog extinction, visibility = 0.2 km

Aerosol Type 10: Desert extinction, visibility based on wind speed

For the 6 aerosol types, the total number of MODTRAN simulations for each surface type is 462,000.~~288,000~~. It is obtained as follows; 6 aerosol types x 100 profiles x 770 angles.

When doing NTB simulation, we use all 6 types of aerosols. The Rural, Ocean, Urban and Fog aerosols are distributed in the lower 0-2 km region. Tropospheric aerosol is distributed from 0 to 10 km tropopause. The Rural, Ocean, Urban and Tropospheric aerosol optical properties have Relative Humidity (RH) dependency. The Single Scattering Albedo (SSA) is given on 4 RH grids (0, 70, 80, 99) on a spectral grid

Formatted: Line spacing: 1.5 lines

Formatted: Font: (Default) +Headings CS (Times New Roman), 12 pt, Complex Script Font: +Headings CS (Times New Roman), 12 pt

Formatted: Font: (Default) +Headings CS (Times New Roman), 12 pt, Complex Script Font: +Headings CS (Times New Roman), 12 pt of 788 points ranging from 0.2 to 300 microns. ~~The Desert aerosol is wind speed dependent and the optical properties are given for 4 wind speeds (0, 10, 20, 30).~~

Simulations were performed for ABI for all the cloud cases described in **Table 3.** To merge cloud layers with atmospheric profiles we have followed the procedure as described in *Berk et al.* (1985, 1998), namely: "Cloud profiles are merged with the other atmospheric profiles (pressure, temperature, molecular constituent, and aerosol) by combining and/or adding new layer boundaries. Any cloud layer boundary within half a meter of an atmospheric boundary layer is translated to make the layer altitudes coincide; new atmospheric layer boundaries are defined to accommodate the additional cloud layer boundaries." 100% relative humidity is assumed within the cloud layers (default).

2.4 Selection of angles

The total number of angles used in the simulations is given in **Table 4**. The selected spectral grids for solar zenith angles, satellite view angles and relative azimuth angles are at Gaussian quadrature points, plus 0º to solar zenith angles (sza) and satellite viewing angles (vza) and 0º and 180º (forward and backward view) to the satellite relative azimuth angles. Solar angle and satellite view angle are referenced to target or surface for satellite simulation with 0º meaning looking up (zenith). Relative a~~A~~zimuth angle is defined as when the relative azimuth angle equals 180º, the sun is in front of observer.

The definitions of solar zenith angle and azimuth angle in this table corresponds to the definitions of MODTRAN but that is not the case for the satellite zenith angle. MODTRAN uses nadir angle as 180º-satellite zenith angle, ignoring spherical geometry.

2.5 Selection of optimal computational scheme

Computational speed is an issue for simulations that account for multiple scattering. MODTRAN4.3 provides three multiple scattering models (Isaacs, DISORT, and Scaled Isaacs) and three band models at resolutions (1 cm^{-1}, 5 cm^{-1}, and 15 cm^{-1}). The DISORT model (Stamnes et al., 1988) provides the most accurate radiance simulations but the runs are very time consuming. The Isaacs (Isaacs et al. 1987) 2-stream algorithm is fast but oversimplified. The Scaled Isaacs method performs radiance calculations at a small number of atmospheric window wavelengths. The multiple scattering contributions for each method are identified and ratios of the DISORT and Isaacs methods are computed. This ratio is interpolated over the full wavelength range, and finally, applied as a multiple scattering scale factor in a spectral radiance calculation performed with the Isaacs method.

To optimize simulation speed and accuracy, we performed various sensitivity tests, including combinations of multiple scattering models, band resolution, and number of streams. **Table 5** lists simulation options and their corresponding calculation speed. The most computationally extensive option is DISORT 8-stream with 1 cm^{-1} resolution which requires 930 seconds to finish one single run. The fastest is Scaled Isaacs with 15 cm^{-1} resolution which only needs 6.67 seconds. Number of streams does not affect the Scaled Isaacs calculation speed. This is different from Isaacs and DISORT for which both stream number and band resolution have notable effects.

Based on results presented in **Table 5**, the efficient options (< 40 seconds) are Isaacs, DISORT 2-stream with 15 cm^{-1}, DISORT 4-stream 15 cm^{-1}, and Scaled Isaacs all streams at all resolutions. Although the ideal option is DISORT 8-stream with 1 cm^{-1} resolution, there is a trade-off between speed and accuracy. **Fig. 6** compares DISORT simulated radiances at three band resolutions. We use two spectral ranges of 0.4 – 0.5 µm and 1.5 – 2.0 µm to illustrate the differences. **Fig. 6** shows that the coarser band resolution has smoothed out the radiance variations. The 15 cm^{-1} has the smoothest curve among the three, and 1 cm^{-1} shows more variations than the other two. Another (scientific) criteria for selecting the spectral resolution is the ability to resolve/match the relative spectral response function (SRF) of a sensor. For example, the SRFs of channels 1-6 of ABI are given at every 1 cm^{-1}.

Accordingly, we have chosen the 1 cm^{-1} band model for the MODTRAN radiance simulations. Performed were also radiance simulations from different multiple scattering models at 1 cm^{-1} resolution. The whole spectrum of 0.2 – 4 µm was separated to 14 sections so that the differences can be assessed clearly. For wavelength below 0.3 µm and beyond 2.5 no discernible differences were found among Isaacs, DISORT 2-, 4-, and 8-strem, and Scaled Isaac. The largest differences occurred in the spectral range of 0.4 – 1.0 µm. Scaled Isaac 8-stream follows DISORT 8-stream closely across the whole spectral range; the Scaled Isaac method provided near-DISORT accuracy with the speed of Isaacs. Thus, the MODTRAN4.3 simulations for GOES-R ABI were set-up with Scaled Isaac 8-stream with 1 cm^{-1} band resolution.

For illustration, in **Fig. 7** compared are radiances simulated by Isaac 2 stream, Scaled Isaac, and DISORT-4 stream for the case of Relative Azimuthal Angle=1.9^{o}, View Angle=76.3^{o}, Solar Zenith Angle=87.2^{o}. The lines are differences between various settings and DISORT-8 stream (e.g. Isaacs minus DISORT-8). Isaac has the least accuracy since it is oversimplified, 4-stream showed some improvements when compared with Isaac while still has large differences for 0.4 µm and is still computationally demanding. Scaled Isaac provides the smallest differences between DISORT-8. **Fig. 6** (lower) zoomed in to the large difference area of 0.3-0.35 µm which indicates that Scaled Isaacs still provides satisfactory results.

2.6 Regression methodologies

We have derived coefficients of regression using a constrained least-square curve fitting methods of Matlab, "lsqnonneg", which can solve a linear or nonlinear least-squares (data-fitting) problem and produce non-negative coefficients. Non-negative coefficients avoid generating negative TOA flux, which is not a physically valid.

To ensure that information from all channels is used and avoid the complex cross-correlation problem, it was opted to generate Narrow to Broad (NTB) coefficients for each ABI channel separately ~~(using "lsqnonneg")~~. These channel specific NTB coefficients are applied to each channel to convert ABI narrow-band reflectance to extended band. The final broad-band TOA reflectance is taken as the weighted sum of all 6-channel specific broad-band reflectance. The logic behind this approach is the assumption that the narrow-band reflectance from each channel is a good representative for a limited spectral region centered around the channel and the total spectral reflectance is dominated by the spectral region that contains the most solar energy

Formatted: Font: (Default) +Headings CS (Times New Roman), Complex Script Font: +Headings CS (Times New Roman)

Formatted: Line spacing: 1.5 lines

We have derived coefficients of regression using a non-constrained and constrained least-square curve fitting methods of Matlab "stepwisefit" and "lsqnonneg". The first one does is a stepwise regression by adding terms to and removing terms from a multilinear model based on their statistical significance. It may give negative coefficients that results in a negative TOA flux, which is not a physically valid result. Subsequently, we have re-derived all the coefficients with "lsqnonneg" which can solve a linear or nonlinear least-squares (data-fitting) problem and produce non-negative coefficients.

To ensure that information from all channels is used and avoid the complex cross-correlation problem, it was opted to generate Narrow to Broad (NTB) coefficients for each ABI channel separately (using "lsqnonneg"). These channel specific NTB coefficients are applied to each channel to convert ABI narrow-band reflectance to extended band. The final broad-band TOA reflectance is taken as the weighted sum of all 6-channel specific broad-band reflectance. The logic behind this approach is the assumption that the narrow-band reflectance from each channel is a good representative for a limited spectral region centered around the middle of the channel and the total spectral reflectance is dominated by the spectral region that contains the most solar energy.

To generate "separate-channel" NTB coefficients, each narrow-band ABI channel reflectance is converted to a reflectance $\rho_{bb,i}$ separately,

$$\rho_{bb,i}(\theta_0, \theta, \phi) = c_{0,i}(\theta_0, \theta, \phi) + c_{1,i}(\theta_0, \theta, \phi) * \rho_{nb,i}(\theta_0, \theta, \phi) \qquad (4)$$

where $\rho_{bb,i}$ is the band reflectance for an interval around each channel i; $c_{0,i}$ and $c_{1,i}$ are regression coefficients for channel i. These regression coefficients are derived separately for various combination of surface, cloud and aerosol types.; The total shortwave broad band (0.25 – 4.0μm) reflectance ρ_{bb}^{est} is obtained by taking the weighted sum of all 6 $\rho_{bb,i}$ reflectance

$$\rho_{bb}^{est}(\theta_0, \theta, \phi) = \sum_i \rho_{bb,i}(\theta_0, \theta, \phi) \frac{S_{0,i}}{S_0} \qquad (5)$$

Here, S_0 and $S_{0,i}$ are total solar irradiance and band solar irradiance for each channel, respectively. Band edges around the six ABI channels are: 49980,–-18723, 18723-13185, 13185-9221, 9221-6812, 6812-

Formatted: Highlight
Formatted: Highlight
Formatted: Highlight
Formatted: Highlight
Formatted: Highlight

5292, 2500 cm^{-1} (0.2001-0.5341, 0.5341-0.7584, 0.7584-1.0845, 1.0845-1.4680, 1.4680-1.8896, 1.8896-4.0000 µm).The corresponding band solar irradiance values are 364, 360, 287, 168, 91, 87 W m^{-2}. **Fig. 8** shows the sensor response function (SRF) and locations of the six ABI channels.

Coefficients are generated for clear condition and 3 types of cloudy conditions. Comparison between ABI TOA flux and CERES products are shown in ~~Figure~~ **Fig. 9**. The "separate-channel" coefficients work well for predominantly clear sky **(Fig.10)**. Differences are somewhat more scattered for cloudy cases. The reason may be due to the fact that the ABI observation time and CERES product time do not match perfectly since cloud condition change quickly. As discussed in Gristey et al. (2019) there are SW spectral reflectance variations for different cloud types. Possibly, for ABI bands some spectral variations associated with cloud variability are missed. It is important to have the correct cloud properties to be able to select correct ADM. Misclassification of cloud properties will therefore result in flux differences. They also argue that ADMs have an uncertainty due to within-scene variability and within-angular bin variability leading to additional flux differences.

3.0 Data used

3.1 Satellite data for GOES-16 and GOES17

The GOES Imager data used **(Table 6)** were downloaded from https://www.bou.class.noaa.gov/ and the SRF from https://ncc.nesdis.noaa.gov/GOESR/ABI.php

* The CODC data were not always available from CLASS and had to be obtained from NOAA/STAR temporary archives. Also, not all the required angular information needed for implementation of regressions was available online and had to be recomputed.

Commented [RTP1]: Something seems missing here.

Formatted: Highlight

Formatted: Not Superscript/ Subscript

Formatted: Font: (Default) +Headings CS (Times New Roman), Complex Script Font: +Headings CS (Times New Roman)

Formatted: Line spacing: 1.5 lines

Formatted: Font: (Default) +Headings CS (Times New Roman), Bold, Complex Script Font: +Headings CS (Times New Roman), Bold

Formatted: Font: (Default) +Headings CS (Times New Roman), Complex Script Font: +Headings CS (Times New Roman)

Formatted: Font: Bold, Complex Script Font: Bold

Formatted: Font: (Default) +Headings CS (Times New Roman), Complex Script Font: +Headings CS (Times New Roman)

Formatted: Font: (Default) +Headings CS (Times New Roman), 12 pt, Complex Script Font: +Headings CS (Times New Roman), 12 pt

Formatted: Font: (Default) +Headings CS (Times New Roman), Complex Script Font: +Headings CS (Times New Roman)

Formatted: Font: Bold

3.2 Reference data from CERES and-FLASHFlux Level2 (FLASH_SSF) Version 3C

Near real-time CERES fluxes and clouds in the SSF format are available within about a week of observation (Kratz et al., 2014). They do not use the most recent CERES instrument calibration and thus contains some uncertainty. Before GOES data were transferred to the Comprehensive Large Array-data Stewardship System (CLASS) system, the NOAA/STAR archive was holding new data for about a week. Therefore, the initial evaluations had to be done only with data that overlapped in time. The CERES data known as the FLASHFlux Level2 (FLASH_SSF) were available almost in real time and did overlap with GOES. These data were downloaded from:

https://ceres.larc.nasa.gov/products.php?product=FLASHFlux-Level2

Due to these limitations the early comparison was done between ABI data as archived at NOAA/STAR and the FLASHFlux products. The archiving of GOES-R at the NOAA Comprehensive Large Array-data Stewardship System (CLASS) started only in 2019 however, it contains data starting from 2017. Once the CLASS archive became available, we have augmented GOES-16 cases with observations from GOES-17; only those cases will be shown in this paper.

3.3 Data preparation

For the re-mapping, we adopted the ESMF re-gridding package. The detailed information can be found at:

http://earthsystemmodeling.org/regrid/

Formatted: Line spacing: Double

For an ideal situation, the ABI high-resolution TOA SW fluxes should be mapped into the CERES footprint for validation as suggested by the Reviewer. However, there are reasons that make it difficult to do so. For example, the case 12/26/2019 UTC 19. There can be more than 18000 pixels in a single swath of the SSF, when constrained to U.S. Different pixels have different times. Neglecting the seconds, there are still more than 30 mins differences (this changes case by case) between the first pixel and the one at the end and this brings up a time matching time issue. But if remapping the SSF to ABI, we can set up a unique time for ABI (ABI is at 5 min intervals) and then constrain the region and the time range of SSF. Both remapping the ABI to SSF and remapping SSF to the ABI bring up spatial matching errors as recognized by the scientific community. In **Fig. 11**, we show the SSF before re-gridding (Figs 11 (a) & (b)) and after re-gridding (Figs. 11 (c) and (d)). The fluxes after re-mapping CERES SSF to the ABI resolution resemble well the original mapping. Another consideration is the computational efficiency of re-mapping the curvilinear tripolar grid to unconstructed grid. For large arrays, it is more efficient to remap the unconstructed grid to the curvilinear tripolar grid.

~~The CERES FLASHFlux_SSF data are re-gridded to match ABI spatial resolution by bi-linear interpolation method from the Earth System Modeling Framework (ESMF) package. The full description of the package can be found via http://earthsystemmodeling.org/regrid/#overview. The time difference between CERES FLASHFlux_SSF and GOES-16 data must be less than ±5 min. e.g., if the GOES-R scanning time is 18:51, then the scripts search the FLASHFLUX points between 18:46~18:56, and use~~

Formatted: Font: Bold, Complex Script Font: Bold the re-gridding method mentioned above to remap the FLASHFLUX to the GOES-R (2 km) domain. Several cases will be illustrated.

The statistics are based on all available points in overlap area. No outliers are removed. All sky, clear sky only, and cloudy only are compared for dates randomly selected. The hour was selected when both GOES-16 and GOES-17 had overlap with CERES FLASHFlux_SSF (Aqua/Terra) data. The coefficients for GOES-17 were obtained by replacing the GOES-16 spectral response function (SRF) by the GOES-17 SRF. All the regressions have been repeated for GOES-17. The GOES-17 SRF was downloaded from https://ncc.nesdis.noaa.gov/GOESR/ABI.php. Simultaneous evaluation for both satellites was performed. The evaluations against the CERES FLASHFlux_SSF data is at footprint scale and covers one hour. The GOES-16 and 17 CONUS data have 5 min intervals, and there are 12 cases in one hour; this requires to test each case independently to find the best time match with CERES FLASHFlux_SSF.

4.0 Results

4.1 Comparison between ABI TOA fluxes to those from CERES SSFand/or FLASHFlux

The CERES Single Scanner Footprint (SSF) is a unique product for studying the role of clouds, aerosols, and radiation in climate. Each CERES footprint (nadir resolution 20-km equivalent diameter) on the SSF includes reflected shortwave (SW), emitted longwave (LW) and window (WN) radiances and top-of-atmosphere (TOA) fluxes from CERES with temporally and spatially coincident imager-based radiances, cloud properties, and aerosols, and meteorological information from a fixed 4-dimensional analysis provided by the Global Modeling and Assimilation Office (GMAO). Each file in this data product

Formatted: Font: 12 pt, Complex Script Font: 12 pt contains one hour of full and partial-Earth view measurements or footprints at a surface reference level. Detailed information can be found via https://ceres.larc.nasa.gov/data/#ssf-level-2. The FLASHFLUX is in footprint format thus it is a variable in time [flux (time)]. In the matching, points that fall in the ±5 min interval of the GOES-R scanning time are used using bilinear interpolation method to get the values for GOES-R domain (e.g., if the GOES-R scanning time is 18:51, then the scripts search the FLASHFLUX points between 18:46~18:56, and use bilinear interpolation method to do the remapping to GOES-R (2 km) domain). A case for 2019/12/26 (doy 360) UTC 19:36 is illustrated in **Figs. 1011-134.** Statistical summaries, from an extended number of cases are presented in **Table 7**, and cover all four seasons.

Formatted: Font: Not Bold

Formatted: Font: Not Bold

The derivation and evaluation of TOA radiative fluxes as simulated for any given instrument are quite challenging. In principle, there is a need to account for all possible changes in the atmospheric and surface conditions one may encounter in the future. Yet, to know what these conditions are at the time of actual observation when there is a need to select the appropriate combination of variables from the simulations, is a formidable task. Therefore, error can be expected due to discrepancies between the actual conditions and the selected simulations and these are difficult to estimate. The approach we have selected is based on high-quality simulations using a proven and accepted radiative transfer code (MODTRAN) of known configurations and a wide range of atmospheric conditions. We have also selected the best available estimates of TOA radiative fluxes from independent sources for evaluation. However, the matching between different satellites in space and time is challenging. In selecting the cases for evaluation, we have adhered to strict criteria of time and space coincidence as described in section 3.3.

We have conducted several experiments to select an appropriate regression approach to the NTB transformation ensuring that non-physical results are not encountered. Based on the samples used in this study **(Table 7)** the differences found for Terra and GOES-16 were in the range of -0.5-(-12.10) for bias and 43.28-82.09 for standard deviation; for Terra and GOES-17 they were 10.81-48.17 and 70.25-109.19, respectively. For Aqua and GOES-16 they were 7.02-29.66 and 45.55-109.08 respectively while for Aqua and GOES-17 they were 0.19-26 and 53.08-94.90, respectively (all units are W m^{-2}). The evaluation

Formatted: Font: Bold

process revealed the challenges in undertaking such comparisons. Both estimates of TOA fluxes (CERES and GOES) do no account for seasonality in the land use classification; the time matching for the different satellites is important and limits the number of samples that can be used in the comparison. Based on the results of this study recommendation for future work include the need to incorporate seasonality in land use and spectral characteristic of the various surface types. Possible stratification by season in the regressions could also be explored.

4.2 Causes for differences between ABI and CERES TOA fluxes

4.2.1 Differences in surface spectral reflectance

In the MODTRAN simulations we use the spectral reflectance information on various surface types as provided by MODTRAN. MODTRAN version 4.3.1 contains a collection of spectral surface reflectance dataset from the Moderate Spectral Atmospheric Radiance and Transmittance (MOSART) model (Cornette et al., 1994) and others from Johns Hopkins University Spectral Library (Baldridge et al., 2009). When doing simulation, we call the built-in surface types and use the provided surface reflectance. As such, the spectral dependence of the surface reflectance used in the simulations and matched to the CERES surface types may not be compatible with the classification of CERES. Also, seasonal changes in surface type classification can in~~yto~~troduce errors du~~t~~e to changes in the spectral surface reflectance~~s~~ for different surface types (Fig. 1~~4~~5).~~,~~

4.2.2 Issues related to surface classification

Another possible cause for differences between the TOA fluxes is the classification of surface types as originally identified by the IGBP and used in the simulations. No seasonality is incorporated in the surface type classification ~~and the impact can be illustrated in the following case study~~while such variability is part of the CERES observations.~~.~~ ~~Simulation results for surface type 8 (open shrub) have been checked~~

~~in depth. The average simulated broad-band reflectance is around 0.2. The regression residual for this surface type is reasonably small for sun angle <80 degrees, namely, the fitted broad-band reflectance is very close to the simulated broad-band reflectance. This would indicate that the regressions are performing properly. However, when we applied the regression coefficient to the GOES-16 ABI observations, the calculated TOA broad-band reflectance was around 0.45, which seemed too high. To explain why the coefficient for channel 6 for "open shrub" was high we illustrate the filter function for channel 6 and spectral albedos for open shrub, desert, woody savanna and grassland in **Fig. 14**.~~

~~In **Fig. 15** we show the TOA fluxes for the entire domain using the original IGBP classification (open shrub) in the area of interest and subsequent replacement with a desert surface. Due to seasonal changes in surface properties, "Desert" classification may be more appropriate for the surface type at the time of the observations. This would indicate the need for introducing seasonal variability in the classification of surface types before one selects the representative NTB transformations.~~

4.2.3 Issues related to match-up between GOES-R and CERES

Both Terra and Aqua have sun-synchronous, near-polar circular orbits. Terra is timed to cross the equator from north to south (descending node) at approximately 10:30 am local time. Aqua is timed to cross the equator from south to north (ascending node) at approximately 1:30 pm local time. The periods for Terra and Aqua are 99 and 98 minutes, respectively. Both have 16 orbits per day. CERES on Terra and Aqua optical FOV at nadir is 16 x 32 or 20 km resolution. Terra passes CONUS during 03-06 UTC (US night time), 16-20 UTC (US day time), and Aqua passes CONUS during 07-11 UTC (US night time), 18-22 UTC (US day time).

Both Terra and Aqua have an instantaneous FOV values at SWATH level. There is no perfect overlap, temporally or spatially with ABI data. The ABI radiance and cloud data are on a regular grid of 2*2 km over CONUS at each hour. To use CERES data for evaluation of ABI, there is a need to perform collocation in both time and space.

5.0 Summary

Critical elements of an inference scheme for TOA radiative flux estimates from satellite observations are: 1) transformation of narrowband quantities into broadband ones; 2) transformation of bi-directional reflectance into albedo by applying Angular Distribution Models (ADMs). In principle, the order in which these transformations are executed is arbitrary. However, since well established, observation-based broadband ADMs derived from the Clouds and the Earth's Radiant Energy System (CERES) project already exist, the logical procedure is to do the NTB transformation on the radiances first, and then apply the ADM. This is the sequence that has been followed here. While the road map to accomplish above objectives seems well defined, reaching the final goal of having a stable up-to-date procedure for deriving TOA radiative fluxes from a new instrument like the ABI on the new generation of GOES satellites is quite complicated. ~~The process of preparing for the usefulness of a new satellite sensor needs to be done in advance,~~ Since the final configuration of the instrument becomes known at a much later stage~~. As such~~c, the evaluation of ~~the~~ new algorithms is in a fluid stage for a long time~~. Agreement~~so early evaluation ~~or disagreement~~ with ~~know~~ "ground truth" is not ~~fully informative~~conclusive about ~~on~~ the performance of ~~the~~ new algorithms. ~~to estimate desired geophysical parameters.~~ Additional complication is related to the lack of maturity of basic information needed in the implementation process, such as a reliable cloud screened product which in itself is in a process of development and modifications. The "ground truth", namely, the CERES observations are also undergoing adjustments and recalibration. As such, the process of deriving best possible estimates of TOA radiative fluxes from ABI underwent numerous iterations to reach its current status. An effort was made to deal the best way possible with the fluid situation. All the evaluations against CERES were repeated once the ABI data reached stability and were archived in CLASS and we used the most recent auxiliary information. The prominence of certain issues surfaced from this study itself. One example is the sensitivity to land classification which currently is static. Another issue is related to the representation of real time aerosol optical depth which is important under clear sky conditions. It is believed that only now when NOAA/STAR has a stable aerosol retrieval algorithm, it would be timely to address the aerosol issue in the estimation of TOA fluxes under clear sky.

Data availability. The data are available upon request from the corresponding author.

Author contributions. The investigation and conceptualization were carried out by RTP, IL and JD. YM and WC developed the software. RTP prepared the original draft. All authors contributed to the writing, editing and review of the publication.

Competing interests. The authors declare that they have no conflict of interest.

Disclaimer. Publisher's note: Copernicus Publications remains neutral with regard to jurisdictional claims in published maps and institutional affiliations.

Acknowledgements. We acknowledge the benefit from the use of the numerous data sources used in this study. These include the Clouds and the Earth's Radiant Energy System (CERES) teams, the Fast Longwave and Shortwave Radiative Flux (FLASHFlux) teams, the
University of Wisconsin-Madison, Space Science and Engineering Center, Cooperative Institute for Meteorological Satellite Studies (CIMSS) for providing the SeeBor Version 5.0 data (https://cimss.ssec.wisc.edu/training_data/, and the final versions of the GOES Imager data were downloaded from https://www.bou.class.noaa.gov/. Several individuals have been involved in the early stages of the project whose contribution led to the refinements of the methodologies. These include M. M. Woncsick and Shuyan Liu. We thank the anonymous Reviewers for a very thorough and constructive comments that helped to improve the manuscript. We thank the Editor Sebastian Schmidt for overseeing the disposition of the manuscript.

Financial support. This research was supported by NOAA/NESDIS GOES-R Program under grants 5275562 1RPRP_DASR and 275562 RPRP_DASR_20 to the University of Maryland.

Formatted: Justified

Formatted: Font: (Default) +Headings CS (Times New Roman), Complex Script Font: +Headings CS (Times New Roman)

Formatted: Font: (Default) +Headings CS (Times New Roman), Complex Script Font: +Headings CS (Times New Roman)

Reference:

Akkermans Tom and Nicolas Clerbaux, 2020. Narrowband-to-Broadband Conversions for Top-of-Atmosphere Reflectance from the Advanced Very High-Resolution Radiometer (AVHRR) *Remote Sens.* 2020, *12* (2), 305; https://doi.org/10.3390/rs12020305

Berk, A., L. W. Bernstein, and D. C. Robertson: MODTRAN: A moderate resolution model for LOWTRAN 7, Philips Laboratory, Report AFGL-TR-83-0187, 1985, Hanscom AFB, MA.

Berk, A., G. P. Anderson, P. K. Acharya, D. C. Robertson, J. H. Chetwynd, S. M. Adler-Golden: MODTRAN Cloud and Multiple Scattering Upgrades with Application to AVIRIS, Remote Sensing of Environment, 65 (3), 367-375, https://doi.org/10.1016/S0034-4257(98)00045-5, 1998.

Baldridge, A. M., S J. Hook, C. I. Grove, G. Rivera: The ASTER spectral library version 2, Remote Sensing of Environment 113, doi: 10.1016/j.rse.2008.11.007, 2009.

Borbas, E. E., S. Wetzel Seemann, H.-L Huang, J. Li, and W. P. Menzel: Global profile training database for satellite regression retrievals with estimates of skin temperature and emissivity. Proceedings of the XIV, International ATOVS Study Conference, Beijing, China, University of Wisconsin-Madison, Space Science and Engineering Center, Cooperative Institute for Meteorological Satellite Studies (CIMSS), Madison, WI, pp.763-770, 2005.

Clerbaux, N., J. E. Russell, S. Dewitte, C. Bertrand, D. Caprion, B. De Paepe, L. Gonzalez Sotelino, A. Ipe, R. Bantges, and H. E. Brindley: Comparison of GERB instantaneous radiance and flux products with CERES Edition-2 data, Rem. Sens. of Environ., **113**, 102-114. doi: 10.1016/j.rse.2008.08.016, 2009.

Cornette, W. M., P. K. Acharya, D. C. Robertson, and G. P. Anderson: Moderate Spectral Atmospheric Radiance and Transmittance Code *(MOSART)*, Rep. R-057-94 (11–30), La Jolla, CA: Photon Research Associates, 1994.

Gristey, J. J., Su,W., Loeb, N. G., Vonder Haar, T. H., Tornow, F., Schmidt, K. S., Hakuba, M. Z., Pilewskie, P., Russell, J. E.: Shortwave Radiance to Irradiance Conversion for Earth Radiation Budget Satellite Observations: A Review, Remote Sens. **2021**, 13, 2640. https://doi.org/10.3390/rs13132640.

Kato, S., Norman G. Loeb David A. Rutan, Fred G. Rose: Clouds and the Earth’s Radiant Energy System (CERES) Data Products for Climate Research Journal of the Meteorological Society of Japan, 93 (6), 597−612, 2015. DOI:10.2151/jmsj.2015-048,

Kratz, D. P., P. W. Stackhouse Jr., S. K. Gupta, A. C. Wilber, P. Sawaengphokhai, and G. R. McGarragh4: The Fast Longwave and Shortwave Flux (FLASHFlux) Data Product: Single-Scanner Footprint Fluxes, J. Appl. Meteor. Climatol., 53, 1059-1079, doi: 10.1175/JAMC-D-13-061.1, 2014.

Hansen, M. C., R. S. Defries, J. R. G. Townshend and R. Sohlberg: Global land cover classi cation at 1km spatial resolution using a classification tree approach, International Journal of Remote Sensing, 21(6-7):1331 – 1364, DOI:10.1080/014311600210209 https://doi.org/10.1080/014311600210209, 2010.

Harries, J. E., J. E. Russell, J. A. Hanafin, H. Brindley, J. Futyan, J. Rufus, S. Kellock, G. Matthews, R. Wrigley, A. Last, J. Mueller, R. Mossavati, J. Ashmall, E. Sawyer, D. Parker, M. Caldwell, P M. Allan, A. Smith, M. J. Bates, B. Coan, B. C. Stewart, D. R. Lepine, L. A. Cornwall, D. R. Corney,

Formatted: Font: (Default) Times New Roman, 12 pt, Complex Script Font: Times New Roman, 12 pt

Formatted: Font: (Default) Times New Roman, 12 pt, Complex Script Font: Times New Roman, 12 pt

Formatted: Indent: Before: 0", Hanging: 0.5", Line spacing: Double

Formatted: Font: (Default) Times New Roman, 12 pt, Complex Script Font: Times New Roman, 12 pt

Formatted: Font: (Default) Times New Roman, 12 pt, Complex Script Font: Times New Roman, 12 pt

Formatted: Font: (Default) Times New Roman, 12 pt, Complex Script Font: Times New Roman, 12 pt

Formatted: Font: (Default) Times New Roman, 12 pt, Complex Script Font: Times New Roman, 12 pt

Formatted: Font: (Default) Times New Roman, 12 pt, Complex Script Font: Times New Roman, 12 pt

Formatted

Formatted

Formatted

Formatted

Formatted

Formatted

Formatted

Formatted

Formatted

Formatted

Formatted

Formatted

Formatted

Formatted

Formatted

Formatted

Field Code Changed

Formatted

M. J. Ricketts, D. Drummond, D. Smart, R. Cutler, S. Dewitte, N. Clerbaux, L. Gonzalez, A. Ipe,C. Bertrand, A. Joukoff, D. Crommelynck, N. Nelms, D. T. Llewellyn-Jones, G. Butcher, G. L. Smith, Z. P Szewczyk, P E. Mlynczak, A. Slingo, R. P. Allan, and M. A. Ringer: The Geostationary Earth Radiation Budget Project, Bull. Amer. Meteor. Soc. 86 (7): 945, doi: 10.1175/BAMS-86-7-945, 2005.

Isaacs, R. G., W.-C. Wang, R. D. Worsham, and S. Goldenberg, S.: Multiple scattering LOWTRAN and FASCODE models. Applied Optics, 26(7), 1272 – 1281, 1987.

Kato, S., and N. G. Loeb (2005), Top-of-atmosphere shortwave broadband observed radiance and estimated irradiance over polar regions from Clouds and the Earth's Radiant Energy System (CERES) instruments on Terra, J. Geophys. Res., 110, D07202, doi:10.1029/2004JD005308

Laszlo, I., H. Liu, H. -Y. Kim, and R. T. Pinker: GOES-R Advanced Baseline Imager (ABI) Algorithm Theoretical Basis Document (ATBD) for Downward Shortwave Radiation (Surface), and Reflected Shortwave Radiation (TOA), version 3.1, Available at https://www.goes-r.gov/resources/docs.html, 2018.

Laszlo, I., H. Liu, H.-Y. Kim, and R. T. Pinker: Shortwave Radiation from ABI on the GOES-R Series, in *The GOES-R Series*, edited by S. J. Goodman, T. J. Schmit, J. Daniels and R. J. Redmon, pp. 179-191, Elsevier, doi: https://doi.org/10.1016/B978-0-12-814327-8.00015-9, 2020.

Loeb, N. G., N. M. Smith, S. Kato, W. F. Miller, S. K. Gupta, P. Minnis, and B. A. Wielicki: Angular Distribution Models for Top-of Atmosphere Radiative Flux Estimation from the Mission Satellite, Part I: Methodology, Journal of Applied Meteorology, 42 240-265, 2003.

Loeb et al. (2005), Angular distribution models for top-of- atmosphere radiative flux estimation from the Clouds and the Earth's Radiant Energy System Instrument on the Terra satellite. part I: Methodology. J. Atmos. Oceanic Technol., 22:338–351.

Loveland T. R., B. C. Reed, J. F. Brown, D. O. Ohlen, Z. Zhu, L. Yang, J. W. Merchant: Development of a global land cover characteristics database and IGBP DISCover from 1 —km AVHRR data, International Journal of Remote Sensing, 21 (6-7), 1303-1330, 2010.

Niu, X. and Rachel T. Pinker: Revisiting satellite radiative flux computations at the top of the atmosphere, International Journal of Remote Sensing, DOI:10.1080/01431161.2011.571298, 2011.

Scarino et al.: A Web-Based Tool for Calculating Spectral Band Difference Adjustment Factors Derived from SCIAMACHY Hyperspectral Data, IEEE Trans. Geo. Remote Sens., 54, 5, 2016,10.1109/TGRS.2015.2502904.

Stamnes, K., S.-C. Tsay, W. Wiscombe and K. Jayaweera: Numerically stable algorithm for discrete-ordinate-method radiative transfer in multiple scattering and emitting layered media, Applied Optics, 27 (12), 2502–2509, 1988.

Su, W., Corbett, J., Eitzen, Z., and Liang, L.: Next-generation angular distribution models for top-of-atmosphere radiative flux calculation from CERES instruments: methodology, Atmos.

Formatted: Font: (Default) +Headings CS (Times New Roman), 12 pt, Complex Script Font: +Headings CS (Times New Roman), 12 pt

Formatted: Indent: Before: 0", Hanging: 0.5", Space After: 0 pt, Line spacing: Double

Formatted: Indent: Before: 0", Hanging: 0.31"

Formatted: Font: (Default) +Headings CS (Times New Roman), 12 pt, Complex Script Font: +Headings CS (Times New Roman), 12 pt

Formatted: Indent: Before: 0", Hanging: 0.5", Space After: 0 pt, Line spacing: Double

Formatted: Font: (Default) +Headings CS (Times New Roman), 12 pt, Complex Script Font: +Headings CS (Times New Roman), 12 pt

Formatted: Font: (Default) +Headings CS (Times New Roman), 12 pt, Complex Script Font: +Headings CS (Times New Roman), 12 pt

Formatted: Font: (Default) +Headings CS (Times New Roman), Complex Script Font: +Headings CS (Times New Roman)

Formatted: Line spacing: Double

Formatted: Indent: First line: 0.56", Line spacing: Double

Meas. Tech., 8, 611–632, https://doi.org/10.5194/amt-8-611-2015, 2015

Wielicki, B.A.; Doelling, D.R.; Young, D.F.; Loeb, N.G.; Garber, D.P.; MacDonnell, D.G. Climate quality broadband and narrowband solar reflected radiance calibration between sensors in orbit. In Proceedings of the IGARSS 2008 IEEE International Geoscience and Remote Sensing Symposium, Boston, MA, USA, 7–11 July 2008.

Zhang, Taiping, Paul W. Stackhouse Jr., Stephen J. Cox, J. Colleen Mikovitz , Charles N. Long Clear-sky shortwave downward flux at the Earth's surface: Ground-based data vs. satellite-based data, Journal of Quantitative Spectroscopy & Radiative Transfer, 224, 247-260, 2019. www.elsevier.com/locate/jqsrt

Formatted: Font: (Default) +Headings CS (Times New Roman), 12 pt, Complex Script Font: +Headings CS (Times New Roman), 12 pt

Formatted: Font: (Default) +Headings CS (Times New Roman), Complex Script Font: +Headings CS (Times New Roman)

Formatted: Space After: 0 pt, Line spacing: Double

Formatted: Font: (Default) +Headings CS (Times New Roman), Complex Script Font: +Headings CS (Times New Roman)

Formatted: Font: (Default) +Headings CS (Times New Roman), Complex Script Font: +Headings CS (Times New Roman)

Formatted: Font: (Default) +Headings CS (Times New Roman), 12 pt, Complex Script Font: +Headings CS (Times New Roman), 12 pt

Formatted: Font: (Default) +Headings CS (Times New Roman), 12 pt, Complex Script Font: +Headings CS (Times New Roman), 12 pt

Field Code Changed

Formatted: Font: (Default) +Headings CS (Times New Roman), Complex Script Font: +Headings CS (Times New Roman)

Formatted: Font: (Default) +Headings CS (Times New Roman), Complex Script Font: +Headings CS (Times New Roman)

Formatted: Indent: Before: 0.56", Space After: 0 pt, Line spacing: Double

Tables

Table 1. ~~Relevant information for the derivation of SW fluxes from selected satellites:~~ C~~c~~hannel information and spectral bands for ABI.

ABI Band #	*Central wavelength (μm)*	*Spectral band (μm)*
1	VIS 0.47	0.45-0.49
2	VIS 0.64	0.60-0.68
3	~~VIS~~ NIR 0.86	0.847-0.882
4	NIR 1.38	1.366-1.380
5	NIR 1.61	1.59-1.63
6	NIR 2.26	2.22-2.27

Formatted Table

Field Code Changed

Table 2. Surface classification description for IGBP 18 types, IGBP 12 types, CERES clear sky 6 types, and NTB cloudy sky 4 types

IGBP (18 types)	IGBP (12 types)	CERES clear-sky (6 types)	NTB cloudy-sky (4 types)
Evergreen Needleleaf	Needleleaf Forest	Mod-High Tree/Shrub	Land
Deciduous Needleleaf			
Evergreen Broadleaf	Broadleaf Forest		
Deciduous Broadleaf			
Mixed Forest	Mixed Forest		
Closed Shrublands	Closed Shrub		
Woody Savannas	Woody Savannas		
Savannas	Savannas	Low-Mod Tree/Shrub	
Grasslands	Grasslands		
Permanent Wetlands			
Tundra			
Croplands	Croplands		
Open Shrublands	Open Shrub		
Urban and Built-up	Open Shrub	Dark Desert	Desert
Bare Soil and Rocks	Barren and Desert	Bright Desert	
Snow and Ice	Snow and Ice	Snow and Ice	Snow and Ice
Water Bodies	Ocean	Ocean	Water

Formatted Table

Table 2. Surface classification description for IGBP 18 types, IGBP 12 types, CERES clear sky 6 types, and NTB cloudy sky 4 types

<table>
<tr><th>IGBP (18 types)</th><th>IGBP (12 types)</th><th>CERES clear-sky (6 types)</th><th>NTB cloudy-sky (4 types)</th></tr>
<tr><td>Evergreen Needleleaf</td><td>Needleleaf Forest</td><td rowspan="6">Mod-High Tree/Shrub</td><td rowspan="12">Land</td></tr>
<tr><td>Evergreen Broadleaf</td><td>Broadleaf Forest</td></tr>
<tr><td>Deciduous Needleleaf</td><td>Needleleaf Forest</td></tr>
<tr><td>Deciduous Broadleaf</td><td>Broadleaf Forest</td></tr>
<tr><td>Mixed Forest</td><td>Mixed Forest</td></tr>
<tr><td>Closed Shrublands</td><td>Closed Shrub</td></tr>
<tr><td>Open Shrublands</td><td>Open Shrub</td><td>Dark Desert</td></tr>
<tr><td>Woody Savannas</td><td>Woody Savannas</td><td>Mod-High Tree/Shrub</td></tr>
<tr><td>Savannas</td><td>Savannas</td><td rowspan="4">Low-Mod Tree/Shrub</td></tr>
<tr><td>Grasslands</td><td rowspan="2">Grasslands</td></tr>
<tr><td>Permanent Wetlands</td></tr>
<tr><td>Croplands</td><td>Croplands</td></tr>
<tr><td>Urban and Built-up</td><td>Open Shrub</td><td>Dark Desert</td><td>Desert</td></tr>
<tr><td>Cropland Mosaics</td><td>Croplands</td><td>Low-Mod Tree/Shrub</td><td>Land</td></tr>
<tr><td>Snow and Ice</td><td>Snow and Ice</td><td>Snow and Ice</td><td>Snow and Ice</td></tr>
<tr><td>Bare Soil and Rocks</td><td>Barren and Desert</td><td>Bright Desert</td><td>Desert</td></tr>
<tr><td>Water Bodies</td><td>Ocean</td><td>Ocean</td><td>Water</td></tr>
<tr><td>Tundra</td><td>Grasslands</td><td>Low-Mod Tree/Shrub</td><td>Land</td></tr>
</table>

Table 3. The various classes for which NTB coefficients are generated.

Parameter	Clear condition	Cloudy condition
Aerosol or cloud type	6 aerosol types (rural, maritime, urban, tropospheric, fog, desert)	3 cloud types (cirrus, stratocumulus, altostratus)
Optical depth (OD)	Typical VIS (km) values for each aerosol types (no OD grid for each aerosol type). Rural: 23, maritime: 23, urban: 5, tropospheric: 50, fog: 0.2, desert: (default VIS for wind speed 10m/s)	Cirrus: [0, 0.8, 1.2, 1.8, 3.2] Stratocumulus: [0, 0.8, 1.2, 1.8, 3.2, 5.8, 8.2, 15.8, 32.2, 51.8, 124.2] Altostratus: [0, 15.0, 30.0, 50.0, 80.0]
Surface type	12 IGBP surface types	4 types (Water, Land, Desert, Snow/Ice)

Table 4. Angles used in simulations. To be consistent with what is presented in the ABI Shortwave Radiation Budget (SRB) Algorithm Theoretical Basis Documents (ATBD) (Laszlo et al, 2018) the additional angles used in the simulations are not given in this Table.

Angle Type	Angles
Solar Zenith Angle [°]	0.0, 12.9, 30.8, 41.2, 48.3, 56.5, 63.2, 69.5, 75.5, 81.4, 87.2
Satellite Zenith Angle [°]	0.0, 11.4, 26.1, 40.3, 53.8, 65.9, 76.3
Azimuth Angle [°]	0.0, 1.9, 10.0, 24.2, 44.0, 68.8, 97.6, 129.3, 162.9, 180

Table 5. MODTRAN simulation speed test (CPU MHz 2099.929).

Algorithm	Stream	Band Resolution (cm^{-1})	Speed (~seconds)
Isaacs	2	1	40
DISORT	2	1, 5, 15	280, 70, 30
	4	1, 5, 15	560, 120, 40
	8	1, 5, 15	930, 300, 110
Scaled Isaac	2	1, 5, 15	30, 10, 6.67
	4	1, 5, 15	30, 10, 6.67
	8	1, 5, 15	30, 10, 6.67

Table 6. Details on data used as input for calculations.

Short Name	Long Name	MODE	ABI-Channel	Scan Sector	Spatial Resolution
RadC	L1b Radiance	M6	C01-C06	CONUS	5000x3000
AODC	L2 Aerosol	M6	--	CONUS	2500x1500
ACMC	L2 Clear Sky Masks	M6	--	CONUS	2500x1500
ACTPC	L2 Cloud Top Phase	M6	--	CONUS	2500x1500
CODC*	L2 Cloud Optical Depth	M6	--	CONUS	2500x1500

Formatted: Left

Formatted: Left

Formatted: Left

Formatted: Left

Formatted: Left

Table 7. Statistical summary for all selected cases intercompared at instantaneous time scale.

Case	**CERES**	**GOES-R**	**Corr**	**Bias**	**Std**	**RMSE**	**N**
07/31 2019 UTC 19	Terra	G16	0.82	0.81	69.81	69.81	0.22 x10^6
		G17	0.87	29.13	90.10	94.70	1.78 x10^6
	Aqua	G16	0.76	33.87	117.43	122.22	1.58 x10^6
		G17	0.78	31.53	129.42	133.21	0.29 x10^6
09/13 2019 UTC 20	Terra	G16	0.87	-17.37	81.72	83.54	0.13x10^6
		G17	0.71	47.09	108.73	118.48	1.73x10^6
	Aqua	G16	0.76	18.22	108.50	110.02	1.46x10^6
		G17	0.73	25.14	81.95	85.72	0.53x10^6
09/21 2019 UTC 19	Terra	G16	0.85	6.78	66.66	67.00	0.35x10^6
		G17	0.83	26.41	87.64	91.57	1.75x10^6
	Aqua	G16	0.82	29.66	105.09	109.20	1.67x10^6
		G17	0.76	6.03	94.70	94.89	0.15x10^6
09/30 2019 UTC 19	Terra	G16	0.88	4.49	64.79	64.94	0.40x10^6
		G17	0.80	19.35	86.41	88.55	1.74x10^6
	Aqua	G16	0.80	19.87	100.45	102.40	1.69x10^6
		G17	0.72	2.71	91.79	91.83	0.12x10^6

10/23 2019 UTC 19	Terra	G16	0.86	5.84	51.44	51.77	$0.35x10^6$
		G17	0.87	22.47	70.25	73.76	$1.75x10^6$
	Aqua	G16	0.89	17.10	75.95	77.85	$1.67x10^6$
		G17	0.78	8.98	72.52	73.07	$0.15x10^6$
11/08 2019 UTC 19	Terra	G16	0.87	-0.5	43.28	43.28	$0.35x10^6$
		G17	0.82	17.18	71.27	73.31	$1.75x10^6$
	Aqua	G16	0.90	10.08	71.27	71.98	$1.67x10^6$
		G17	0.68	1.53	47.55	47.58	$0.15x10^6$
11/24 2019 UTC 19	Terra	G16	0.79	7.98	49.10	49.75	$0.35x10^6$
		G17	0.87	14.10	78.35	79.61	$1.76x10^6$
	Aqua	G16	0.82	7.63	58.68	59.17	$1.67x10^6$
		G17	0.65	0.19	63.14	63.14	$0.15x10^6$
12/26 2019 UTC 19	Terra	G16	0.88	5.24	53.28	53.54	$0.35x10^6$
		G17	0.76	11.26	73.95	74.80	$1.76x10^6$
	Aqua	G16	0.83	9.79	58.90	59.56	$1.67x10^6$
		G17	0.73	0.85	52.53	52.54	$0.15x10^6$

Table 7. Statistical summary for all selected cases intercompared at instantaneous time scale.

Case	CERES	GOES-R	Corr	Bias	Std	RMSE	N
09/13 2019 UTC 20	Terra	G16	0.87	-12.10	82.09	82.98	$0.13\text{x}10^{6}$
		G17	0.71	48.17	108.19	118.42	$1.73\text{x}10^{6}$
	Aqua	G16	0.76	17.38	109.08	110.45	$1.46\text{x}10^{6}$
		G17	0.73	26.00	81.96	85.98	$0.53\text{x}10^{6}$
09/21 2019 UTC 19	Terra	G16	0.85	6.78	66.66	67.00	$0.35\text{x}10^{6}$
		G17	0.83	26.41	87.64	91.57	$1.75\text{x}10^{6}$
	Aqua	G16	0.82	29.66	105.09	109.20	$1.67\text{x}10^{6}$
		G17	0.76	6.03	94.70	94.89	$0.15\text{x}10^{6}$
09/30 2019 UTC 19	Terra	G16	0.88	4.49	64.79	64.94	$0.40\text{x}10^{6}$
		G17	0.80	19.35	86.41	88.55	$1.74\text{x}10^{6}$
	Aqua	G16	0.81	19.99	99.98	101.96	$1.67\text{x}10^{6}$
		G17	0.70	1.22	94.90	94.91	$0.12\text{x}10^{6}$
10/23 2019 UTC 19	Terra	G16	0.86	5.84	51.44	51.77	$0.35\text{x}10^{6}$
		G17	0.87	22.47	70.25	73.76	$1.75\text{x}10^{6}$
	Aqua	G16	0.89	17.10	75.95	77.85	$1.67\text{x}10^{6}$
		G17	0.78	8.98	72.52	73.07	$0.15\text{x}10^{6}$
11/08 2019	Terra	G16	0.87	-0.5	43.28	43.28	$0.35\text{x}10^{6}$
		G17	0.82	17.18	71.27	73.31	$1.75\text{x}10^{6}$

UTC 19	Aqua	G16	0.90	10.08	71.27	71.98	1.67x10^6
		G17	0.68	1.53	47.55	47.58	0.15x10^6
11/24 2019 UTC 19	Terra	G16	0.79	7.98	49.10	49.75	0.35x10^6
		G17	0.87	14.10	78.35	79.61	1.76x10^6
	Aqua	G16	0.82	7.63	58.68	59.17	1.67x10^6
		G17	0.65	0.19	63.14	63.14	0.15x10^6
12/26 2019 UTC 19	Terra	G16	0.89	7.6	52.79	53.33	0.35x10^6
		G17	0.77	10.81	73.14	73.93	1.76x10^6
	Aqua	G16	0.83	7.02	59.16	59.58	1.67x10^6
		G17	0.73	-1.09	53.08	53.09	0.15x10^6

Figures

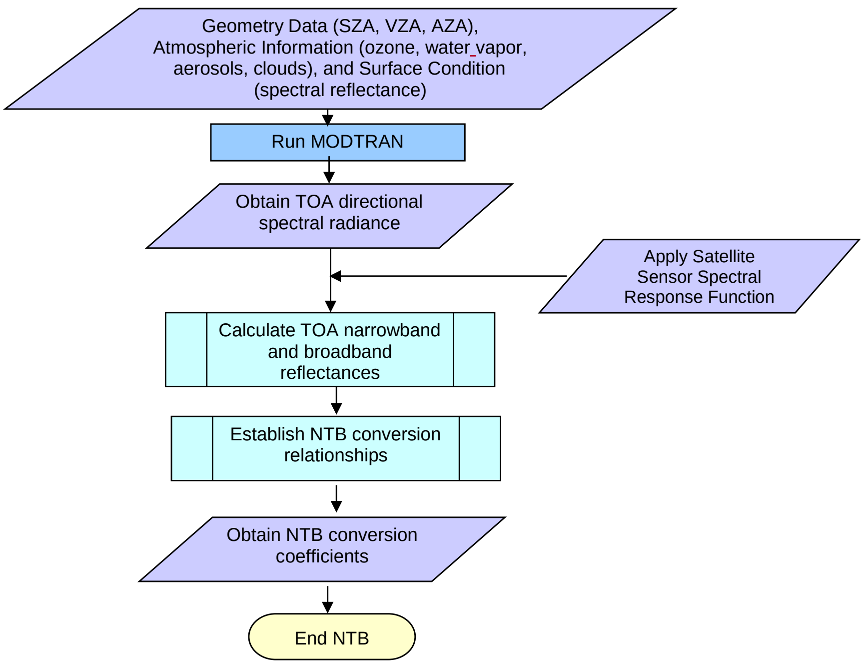

Figure 1. Flowchart of the NTB transformations illustrating the main processing sections.

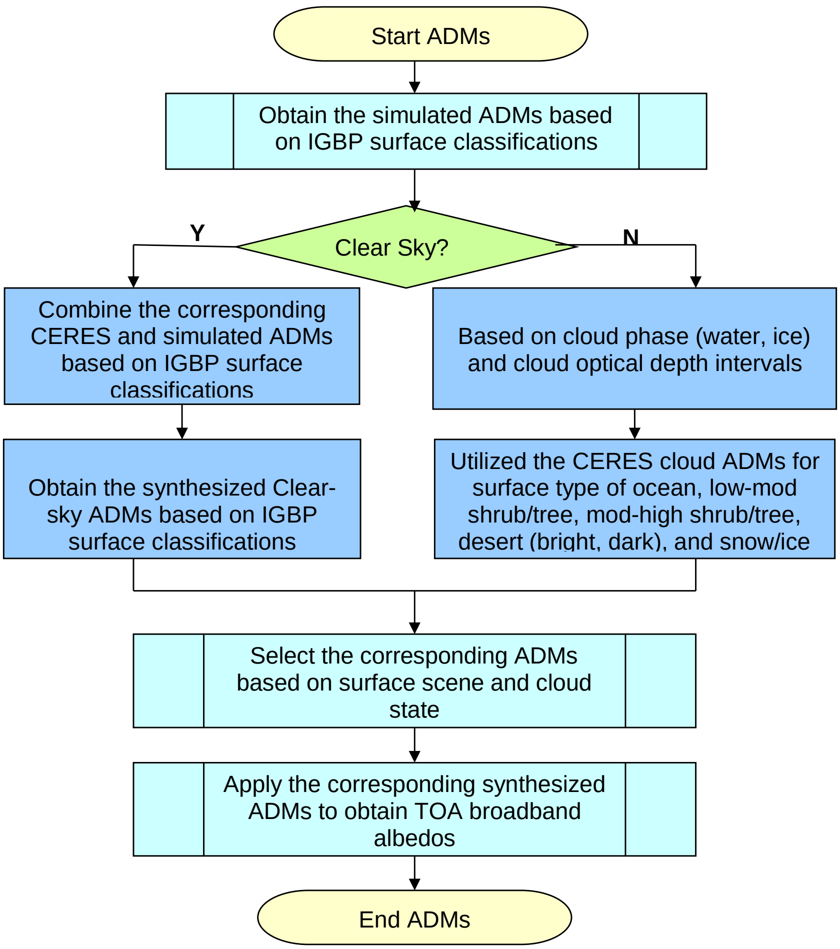

Figure 2. Schematic illustration of the logic employed to synthesize modeled and observed ADMs.

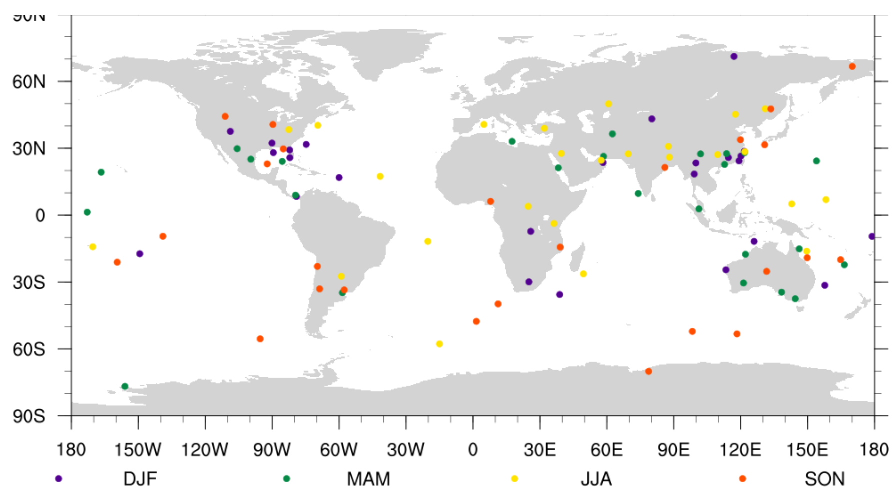

Figure 3. The location of the 100 selected clear sky profiles from SeeBor used in the simulations.

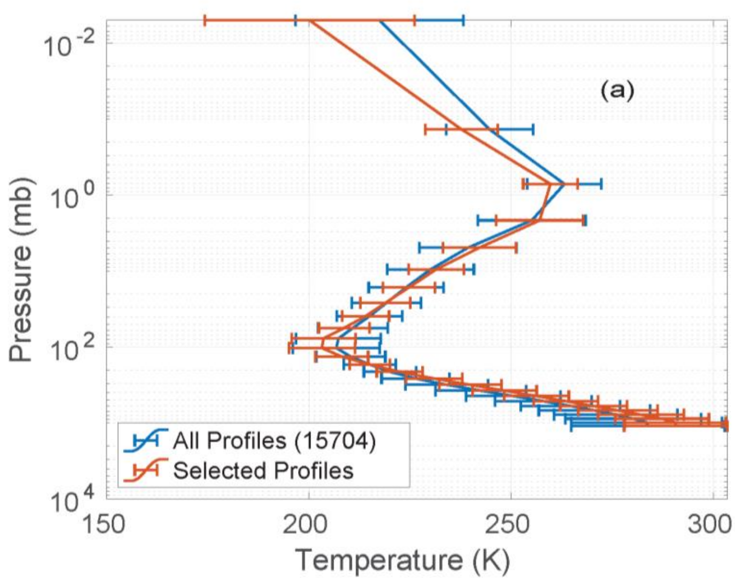

(a)
Pressure (mb)
Temperature (K)
All Profiles (15704)
Selected Profiles

643

644

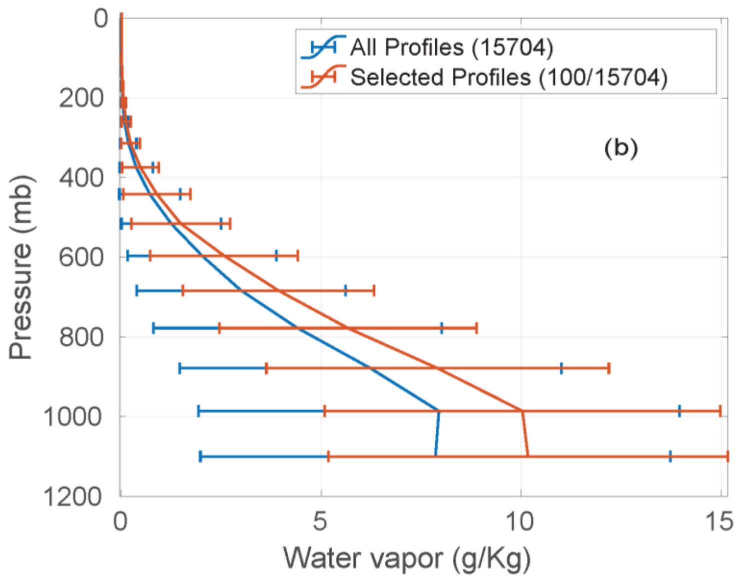

All Profiles (15704)
Selected Profiles (100/15704)
(b)
Pressure (mb)
0
200
400
600
800
1000
1200
0
5
10
15
Water vapor (g/Kg)

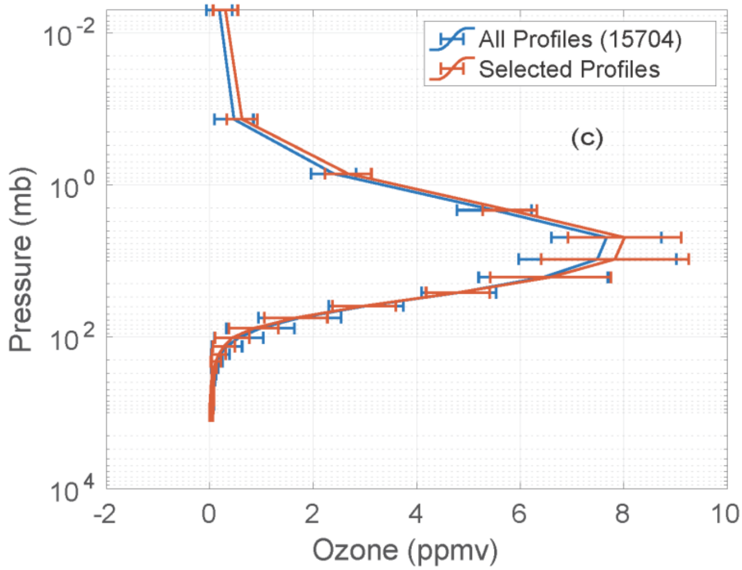

Figure 4. Profile statistics of: (a) temperature; (b): water vapor; (c) ozone for the entire available sample and for the reduced sample used in this study. Error bar is 1 standard deviation. ~~(logarithmic scale).~~

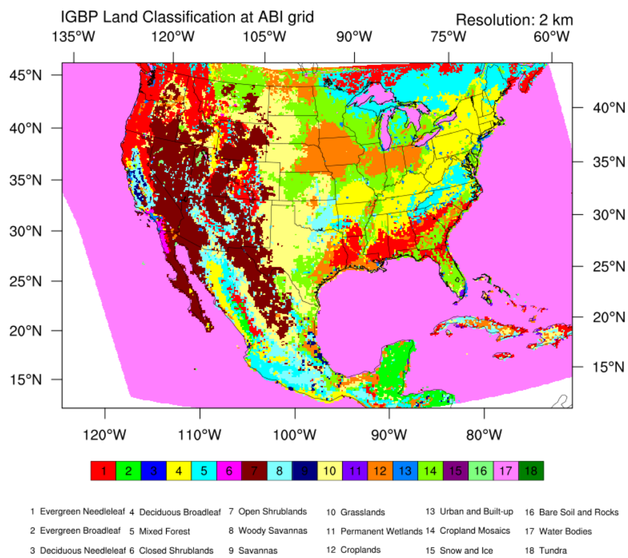

Figure 5. Re-mapped IGBP surface classifications over the CONUS at 2-km ABI grid.

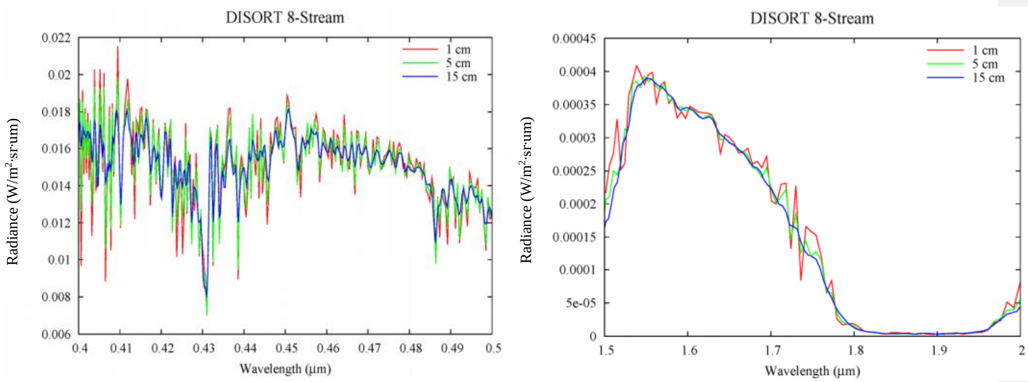

Figure 6. Simulated Radiances from DISORT 8-stream (with 1, 5, and 15 cm^{-1} resolution band model for spectral range of 0.4 – 0.5 µm (left) and 1.5 – 2.0 µm (right).

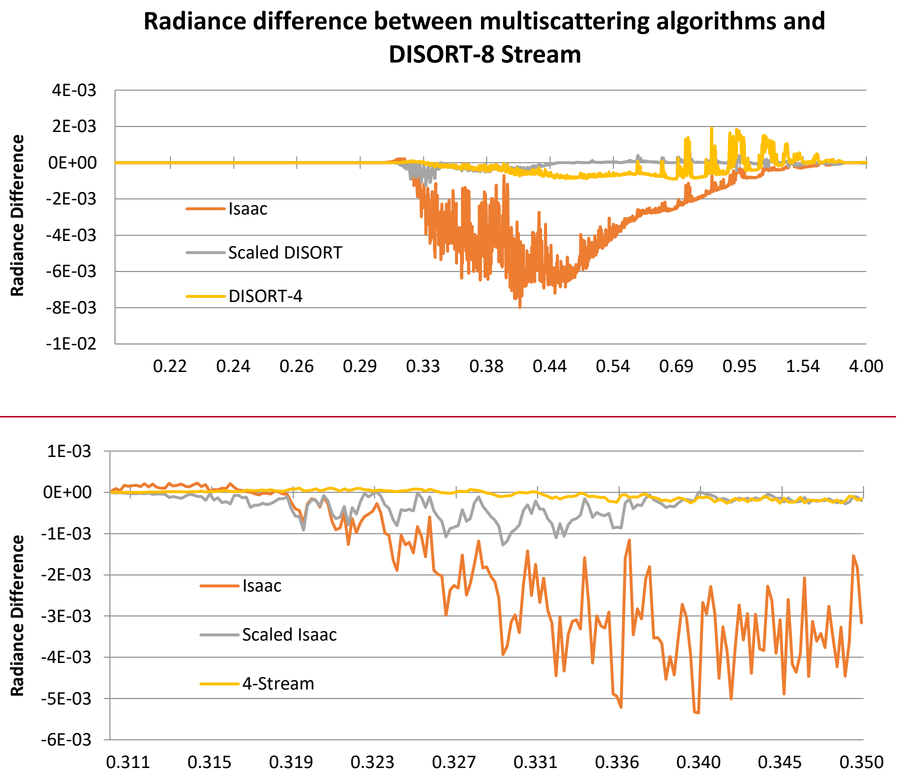

Figure 7. Radiance differences between various multi-scattering algorithms and DISORT-8 stream. *Upper*: the whole simulated spectrum of 0.2-4 μm; *Lower:* zoom on 0.3-0.35 μm (Relative Azimuthal Angle=1.9°, View Angle=76.3°, Solar Zenith Angle=87.2°)

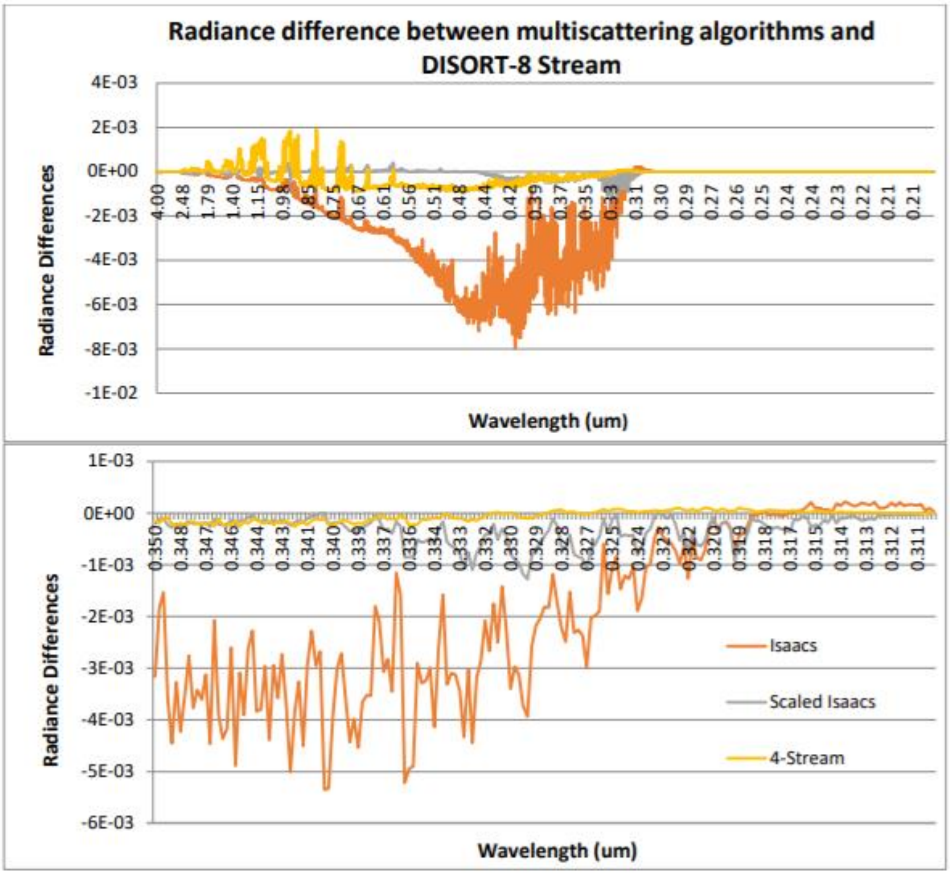
Radiance difference between multiscattering algorithms and DISORT-8 Stream
Radiance Differences
Wavelength (um)
Radiance Differences
Wavelength (um)
Isaacs
Scaled Isaacs
4-Stream

~~Figure 7. Radiance differences between various multi-scattering algorithms and DISORT-8 stream. *Upper*: the whole simulated spectrum of 0.2-4 μm; *Lower:* zoom on 0.3-0.35 μm (Relative Azimuthal Angle=1.9°, View Angle=76.3°, Solar Zenith Angle=87.2°).~~

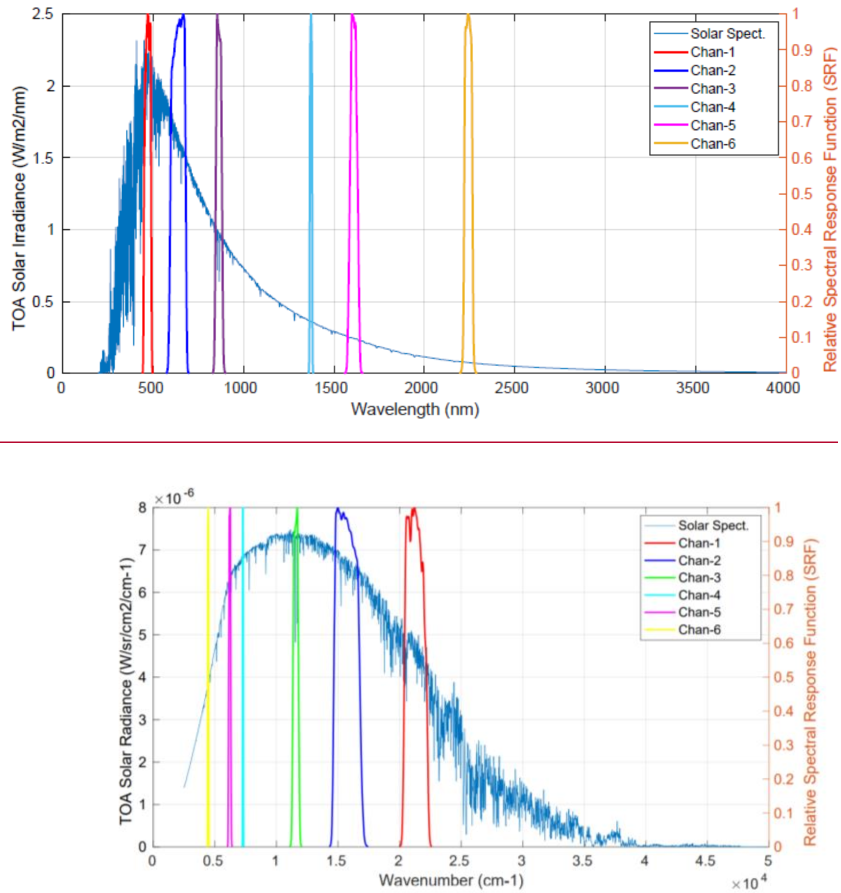

Figure 8. Locations of the six ABI channel SRFs. X-axis is wavenumber. Y-axis is solar irradiance.

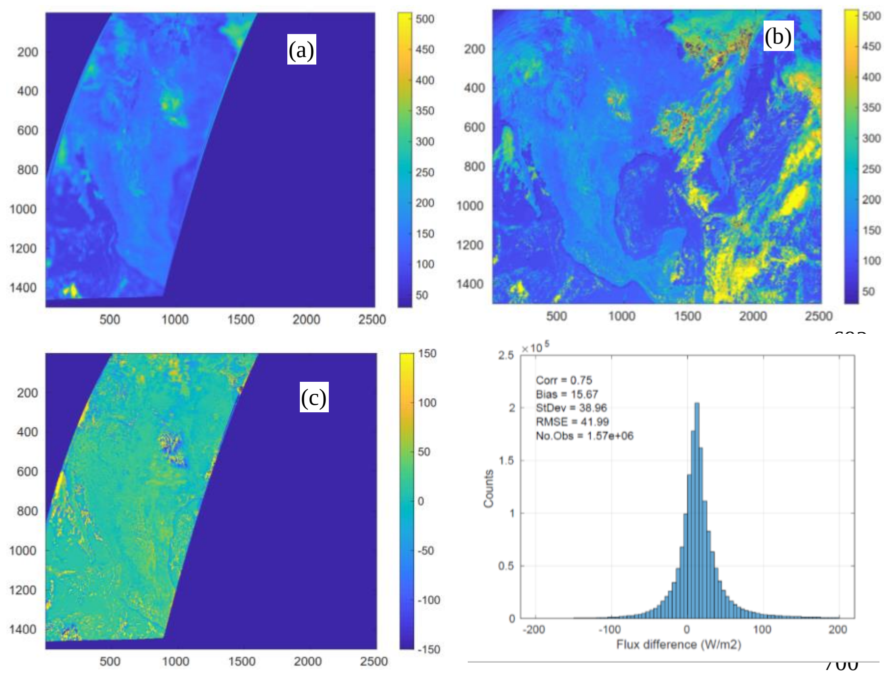

Figure 9. Comparison of TOA flux from ABI and CERES based FLASHFlux for 2017/11/25, 17:57Z. (a) CERES Terra product; (b): results with "separate-channel" coefficients. (c): difference (ABI-CERES); (d): histogram of ABI-CERES differences (this is the only case illustrated in this paper with data from FLASHFlux).

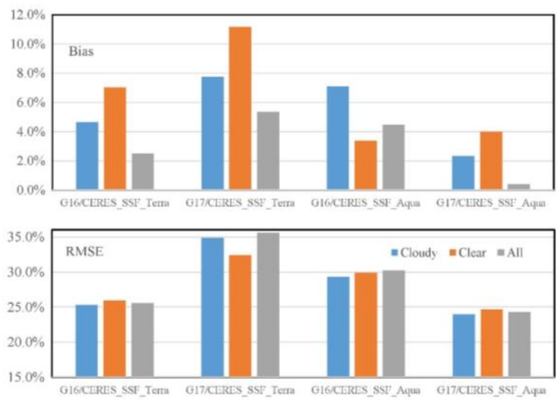

Figure 10. Statistics for rwlative Bias and RMSE. The y-axis is percentage. The x-axis is the case used in the intercomparison. Blue - cloudy orange - clear sky and t gray - all sky.

Formatted: Line spacing: 1.5 lines

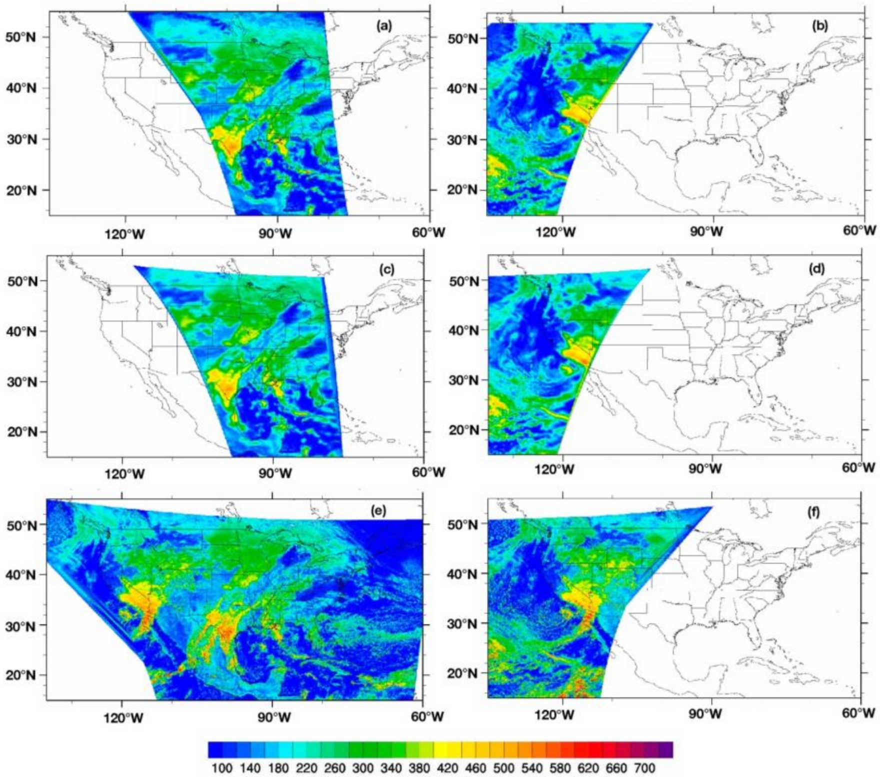

Figure 10. All sky TOA SW from CERES FLASHFlux/Aqua (a), CERES FLASHFlux/Terra (b), re-gridded CERES FLASHFlux/Aqua (c), CERES FLASHFlux/Terra GOES-16 (d) and GOES-17 (f) on 12/26/2019 at UTC 19:36.

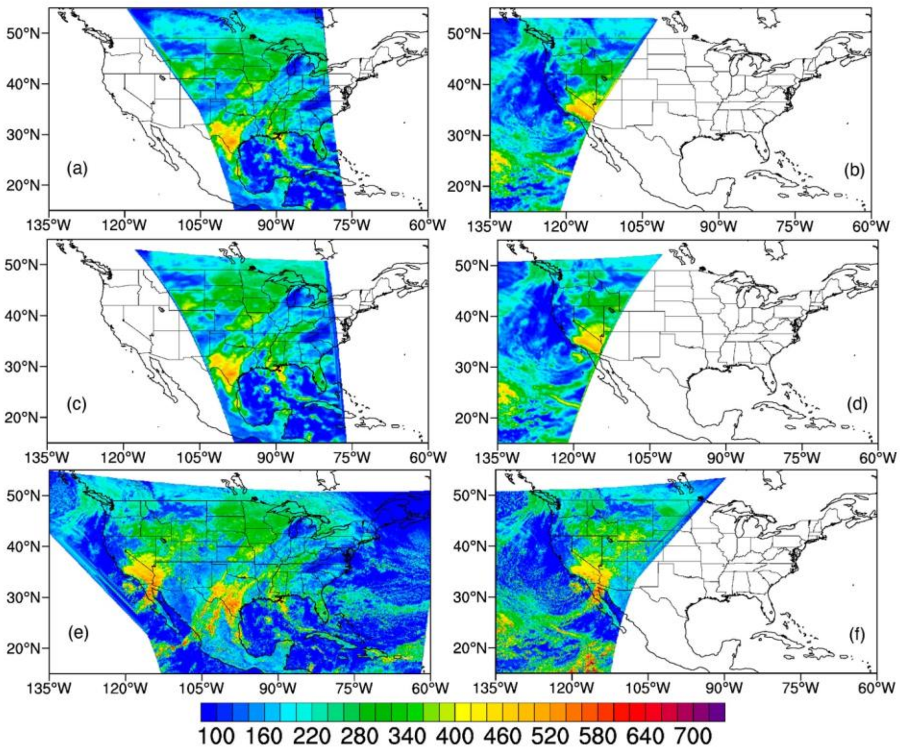

Figure 11. (a) All sky TOA SW from CERES_SSF/Aqua, (b) CERES_SSF/Terra, (c) re-gridded CERES_SSF/Aqua, (d) re-gridded CERES_SSF/Terra, (e) GOES-16 and (f) GOES-17 on 12/26/2019 at UTC 19:36.

Formatted: No underline

Formatted: No underline

Formatted: Not Highlight

Formatted: Line spacing: 1.5 lines

Formatted: Not Highlight

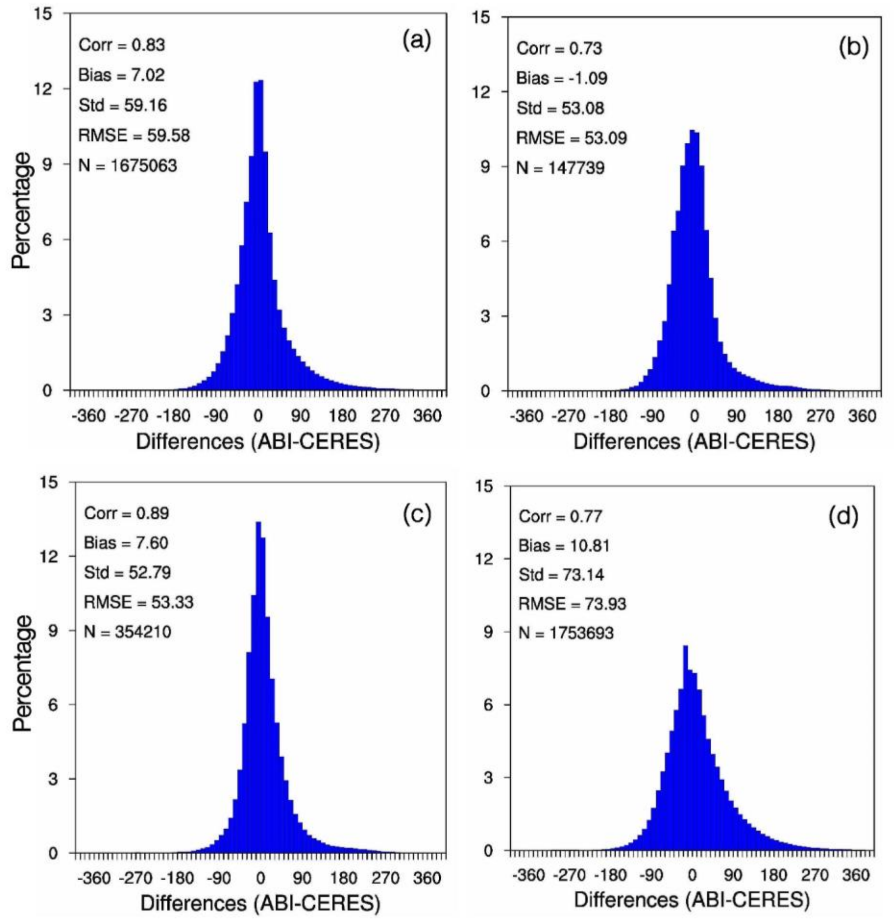

~~Figure 11. Frequency distribution of all-sky TOA SW differences between ABI on GOES-16 and CERES (*Left*) and ABI on GOES-17 and CERES (*Right*) using Aqua (Upper) and Terra (Lower). All observations were used (clear and cloudy) on 12/26/2019 at UTC 19:36.~~

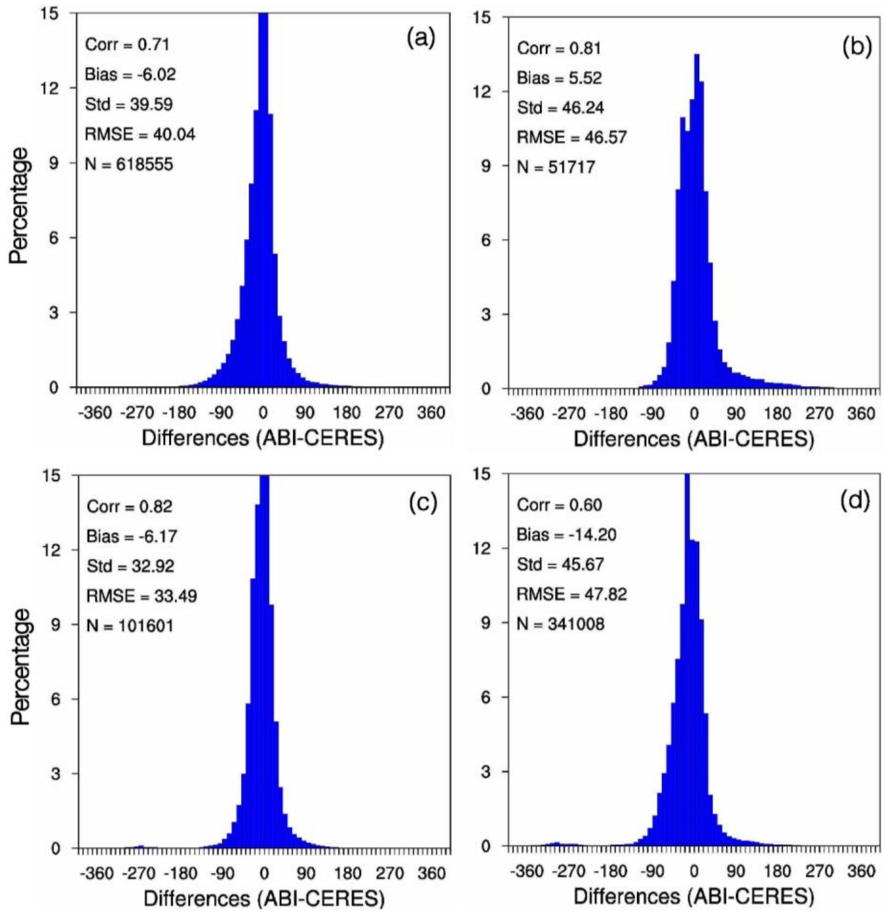

~~Figure 12. Same as Figure 11 but for clear TOA SW differences.~~

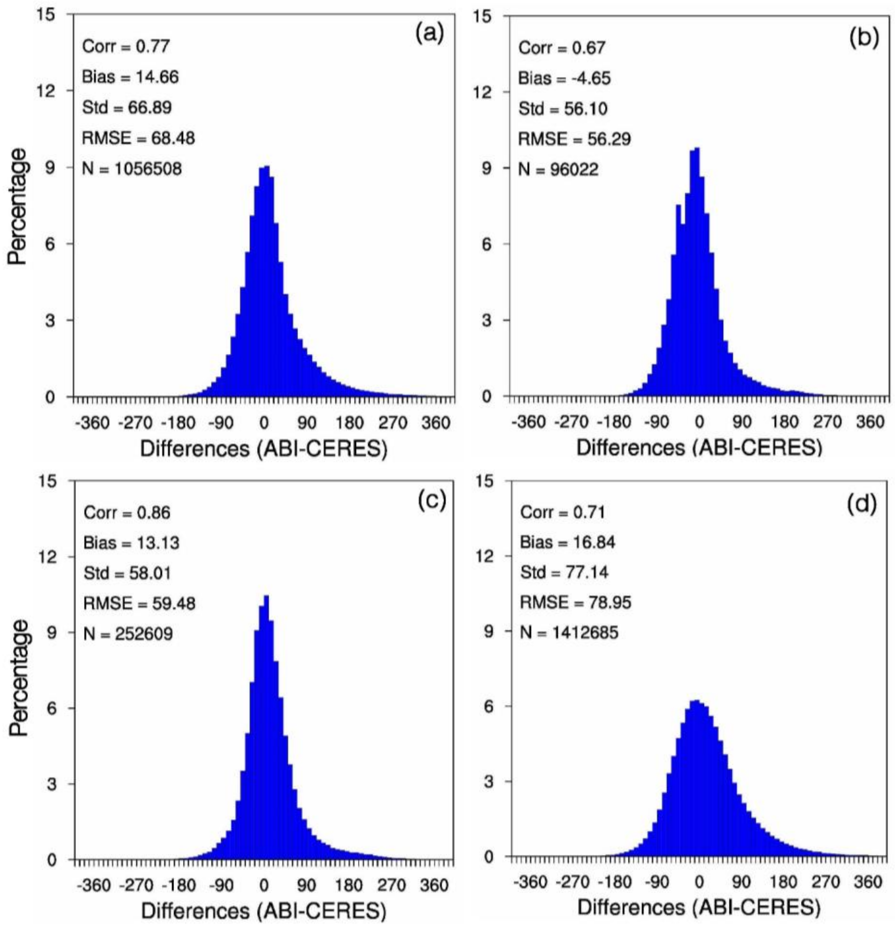

Figure 13. Same as Figure 11 but for cloudy TOA SW differences.

Figure 12. (a) Frequency distribution of all-sky TOA SW differences between ABI on GOES-16 and CERES, (b) ABI on GOES-17 and CERES_SSF using Aqua (Upper) and Terra (Lower). All observations were used (clear and cloudy) on 12/26/

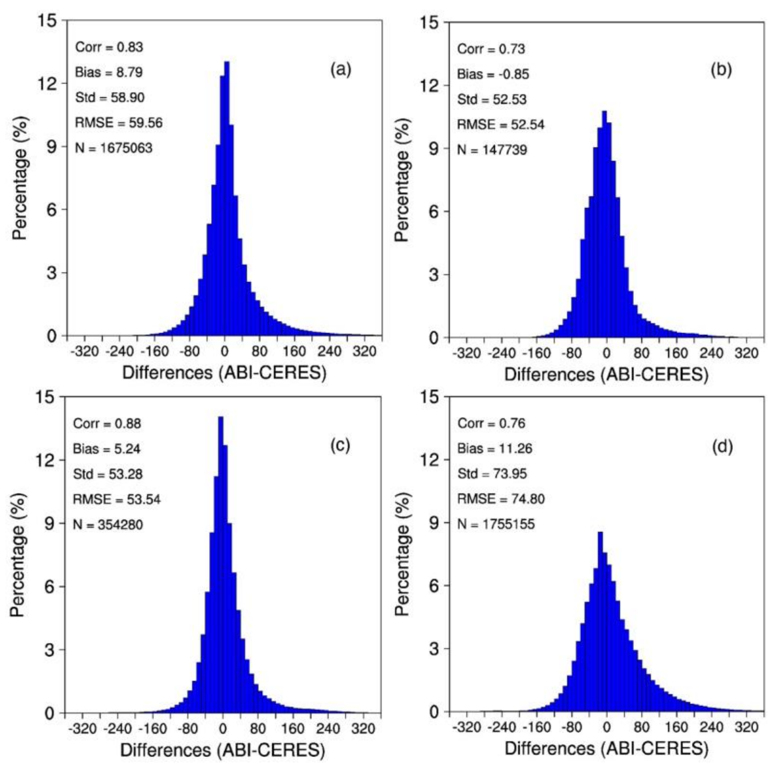

2019 at UTC 19:36.

Formatted: No underline

Formatted: Not Highlight

Formatted: Not Highlight

Formatted: Indent: Before: 0", Hanging: 0.5", Line spacing: 1.5 lines

Formatted: Not Highlight

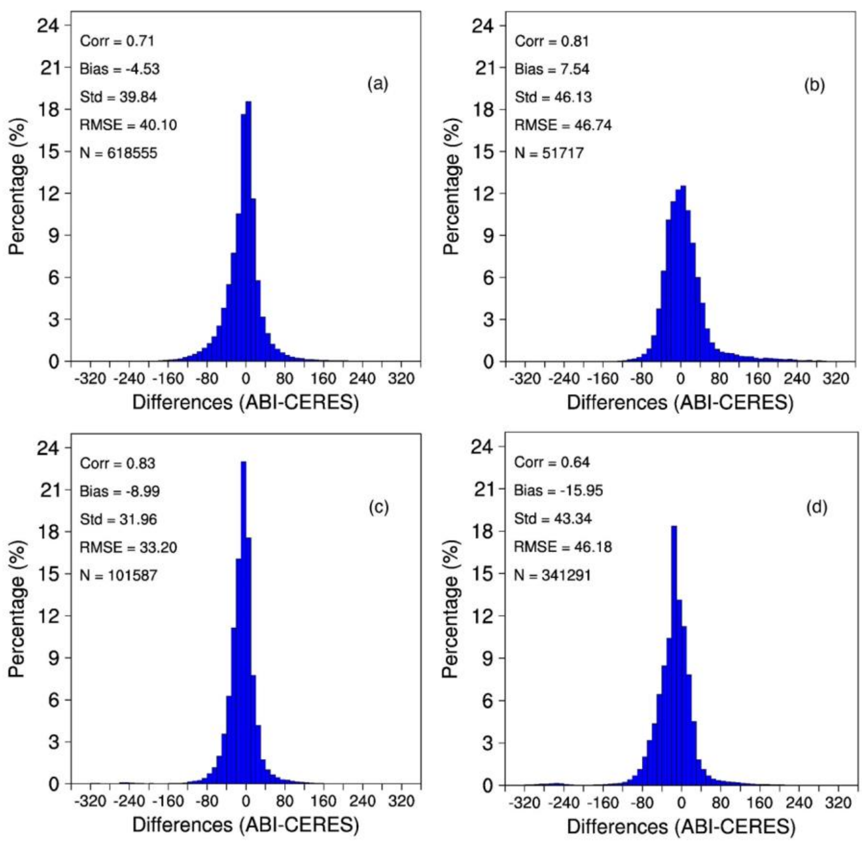

Figure 13. Same as Figure 11 but for clear TOA SW differences.

Formatted: Not Highlight

Formatted: Not Highlight

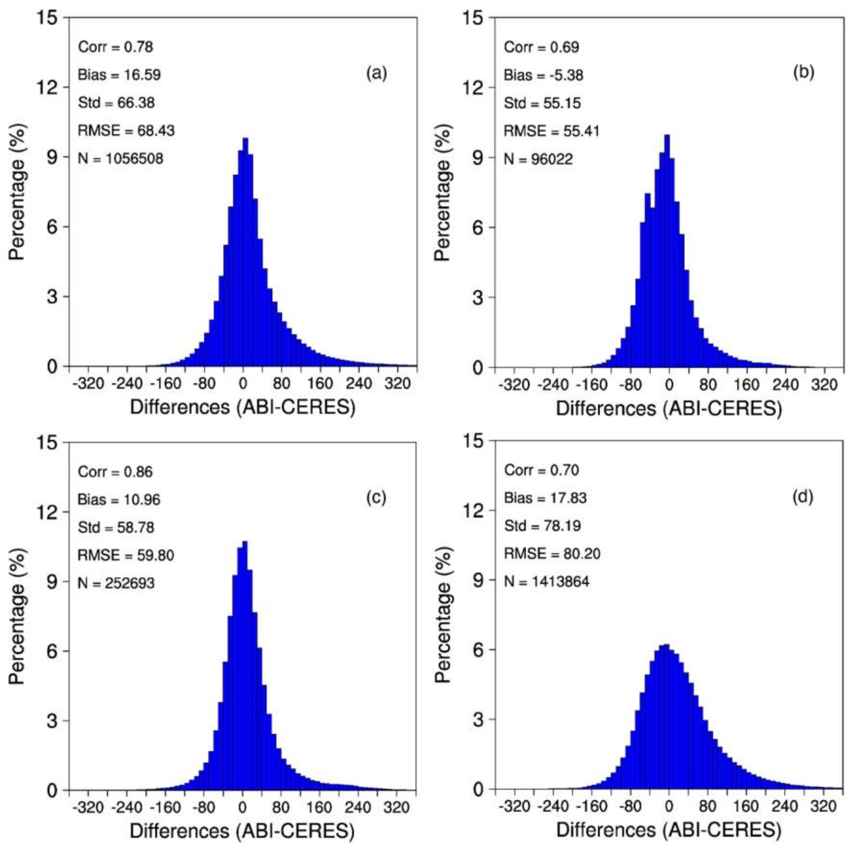

Figure 14. Same as Figure 11 but for cloudy TOA SW differences.

Formatted: Not Highlight

Formatted: Not Highlight

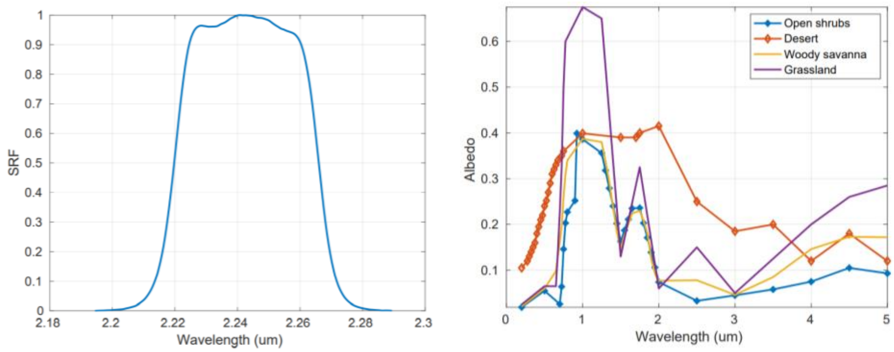

Figure ~~14~~15. *Left:* Sensor response function for ABI channel 6; *Right:* Spectral albedo for desert and open shrubs. Desert albedo value is much higher than open shrubs at 2.2 µm.

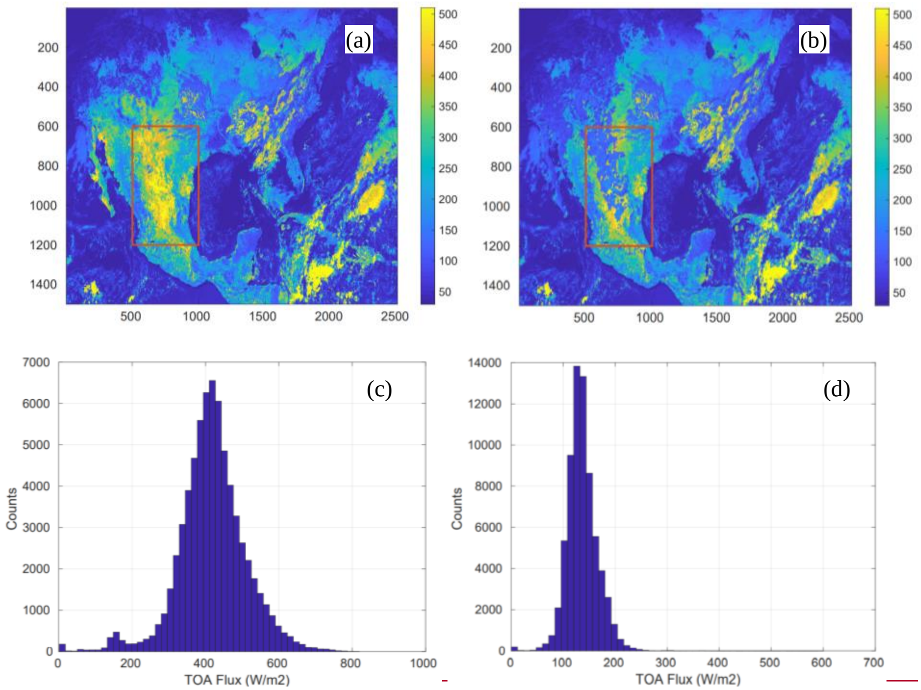

~~**Figure 15**. TOA fluxes using two different NTB coefficients: *Left*: used "open shrub" coefficients; *Right*: "Desert" coefficients. Lower panels show the frequency distribution of TOA fluxes for a reduced domain (over Mexico in the orange boxes) that includes the open shrub/desert classification. Case time stamp is 2017/11/25 17:32Z.~~

Formatted: Space After: Auto, Line spacing: single